

# Two Fluid Quantum Bouncing Cosmology I: Theoretical Model

Sandro Dias Pinto Vitenti,<sup>1,\*</sup> Nelson Pinto-Neto,<sup>2,†</sup> Patrick Peter,<sup>3,‡</sup> and Luiz Felipe Demétrio<sup>1,§</sup>

<sup>1</sup>*Departamento de Física, Universidade Estadual de Londrina,  
Rod. Celso Garcia Cid, Km 380, 86057-970, Londrina, Paraná, Brazil*

<sup>2</sup>*COSMO – Centro Brasileiro de Pesquisas Físicas,  
Rua Dr. Xavier Sigaud 150, 22290-180, Rio de Janeiro – RJ, Brasil*  
<sup>3</sup>*GReCO – Institut d’Astrophysique de Paris, CNRS & Sorbonne Université,  
UMR 7095 98 bis boulevard Arago, 75014 Paris, France*

(Dated: January 23, 2026)

Bouncing cosmologies offer an alternative to inflation by resolving the initial singularity through a contracting phase followed by a bounce into expansion. In many such models, the contracting phase is dominated by a single matter component, typically pressureless dust, which leads to an almost scale-invariant spectrum of scalar cosmological perturbations with a slight blue tilt, so that generating the observed red-tilted spectrum within this framework was challenging. In this work, we consider a more realistic scenario in which the contracting phase includes both matter and radiation, as required on physical grounds. We show that the presence of radiation can naturally induce a red tilt in the spectrum of curvature perturbations seeded by quantum vacuum fluctuations in the remote past of the contraction. Since the perturbations of the two fluids are coupled via gravity, vacuum initial conditions must be carefully defined. We demonstrate that, without fine-tuning, the resulting entropy perturbations are subdominant with respect to curvature perturbations. This suggests that a minimal two-component bounce model, involving only ordinary matter and radiation, can connect to the standard expanding cosmology with observationally viable initial conditions.

PACS numbers: 98.80.Es, 98.80.-k, 98.80.Jk

## I. INTRODUCTION

The matter bounce scenario [1–3] has been proposed as a cosmological model in which the universe initiates in a contracting phase dominated by an almost pressureless fluid, bounces due to quantum effects or corrections to general relativity (GR), and subsequently connects with the standard hot big-bang expanding model. A mapping between these models and an almost de Sitter inflationary expansion have been found [4] and explored in depth [5]. In such a scenario, the spectral index is found to be  $n_s - 1 = 12w/(1 + 3w)$ , where  $w = p/\rho$  is the equation of state parameter relating the fluid pressure  $p$  to its energy density  $\rho$ .

In case the fluid is represented by a canonical scalar field, it is possible to set  $w < 0$  in order to obtain a red-tilted spectral index, as well as  $|w| \ll 1$  to agree with the data. Then, the sound speed of the perturbations satisfies  $c_s^2 = 1$  implying, in most cases, that the ratio  $r = \mathcal{A}_T/\mathcal{A}_s$  between tensor and scalar perturbations amplitudes, is much larger than that observed. This particular problem can however be addressed as, e.g., in Ref. [6], through a relative enhancement of the amplitude of scalar perturbations due to quantum effects near the bounce. Another feature of this model is that the scalar field can also act as a late-time dark energy component,

but only during the expanding phase, hence constituting a bouncing model with a dark energy phase that does not affect the initial conditions posed in the contracting phase.

Assuming the almost pressureless matter is described phenomenologically by a perfect fluid, sometimes modeled by a  $k$ -essence scalar field, the sound speed satisfies  $c_s^2 = w$ , so that tensor perturbations are highly suppressed, satisfying the observed constraints on  $r$ . The fluid could also be understood as dark matter, an observed component of the Universe, which should play an essential role in the contracting phase of the model. If this is the case, there is no addition of an extra unobserved scalar field in the cosmological model, as described in the precedent paragraph and as is required by inflationary models with the inflaton. However, it is physically implausible that such description can allow  $w < 0$ , leading to obvious instabilities, and one must conclude the model to be blue-tilted, contrary to observations.

The aim of this paper is to add some complexity to the matter bounce scenario to make it more realistic by adding the expected radiation-dominated phase at high temperatures, and calculate the consequences in the scalar perturbation theory and the resulting spectral index. We assume both components to be phenomenologically described by fluids, so our model only contains the matter components already observed, namely dark (and ordinary) matter and radiation. Note also that, at small scales, the radiation fluid starts dominating and the background standard model cosmological scenario naturally emerges after the bounce.

The singularity avoidance by means of a bounce stems from the emergence of quantum effects beyond classi-

\* [vitenti@uel.br](mailto:vitenti@uel.br)

† [nelsonpn@cbpf.br](mailto:nelsonpn@cbpf.br)

‡ [peter@iap.fr](mailto:peter@iap.fr)

§ [demetrio.luizfelipe.fis@gmail.com](mailto:demetrio.luizfelipe.fis@gmail.com)

cal GR at small scales. Lacking a satisfactory theory for quantum gravity [7], many effective approaches have been developed to implement a quantum bouncing scenario, like loop quantum cosmology [8, 9], string theory effective actions [10], and the more straightforward canonical quantization of gravity [11]. In the framework of this last approach, we have published a series of papers [3, 12–17] calculating the Hamiltonian constraint up to second order in perturbation theory over homogeneous and isotropic backgrounds for different matter fields (including canonical scalar fields and fluids). Using a proper definition of quantum trajectories [18–20] in configuration space, we were able to show that many quantum trajectory solutions for the background are free of singularities, replaced by a bounce, and reach the classical limit at large scales. The perturbations obey the same equations as in the semi-classical theory (in which only the perturbations are quantized), but with the classical background trajectories substituted by the quantum ones in the relevant equations.

One must however keep in mind that such an approach is not expected to be reliable very close to Planckian energies: the minimum curvature scale of the universe evolution, which is usually reached at the bounce, should thus be sufficiently far from the Planck length. As the relevant distance scales (in appropriate units) are sufficiently large even near the bounce, the matter content of the universe can be adequately approximated by a single perfect fluid with constant equation of state  $w_B$  near the bounce. In practice, in the present case of matter and radiation, one expects radiation domination during this high temperature dense phase, so that  $w_B = w_r = 1/3$ .

In what follows, we first, in Sec. II, summarize our model and compute the quantum corrections to the scale factor evolution as a function of  $w_r$  and the late time parameters, namely the other fluid equation of state  $w$ , and the various relative contributions measured today. Our goal is to describe a model taking care of the observational knowledge of the cosmological parameters, but extended to account for earlier contracting and bouncing phases.

On this well-defined phenomenological background, we evaluate, in Sec. III, the relevant perturbations and their evolution, assuming, as is usual in inflationary models, an initial quantum vacuum state for this many-fluid system [17]. Let us remark at this point that the presence of two fluids in the matter sector leads to coupled scalar perturbations, for which the usual techniques for defining vacuum states cannot be applied. To deal with this problem, we apply the coupled adiabatic vacuum prescription [17] to define an appropriate vacuum state and then calculate the time evolution of the relevant observables (power spectra and correlations) to conclude that, even though we consider a two-fluid situation, the curvature mode largely exceeds the amplitude of the isocurvature contribution and yields an almost scale-invariant and slightly red Gaussian spectrum.

Once placed as a natural extension of the  $\Lambda$ CDM model

consisting of large, classical, dust dominated ( $w \ll 1$ ) contracting and expanding phases smoothly connected by a regular quantum radiation-dominated bounce: a scenario having no free parameter but for the value of the scale factor at its minimum, which we denoted by  $a_B \equiv a(\eta_B)$ , with  $\eta_B$  the conformal time at the bounce. This parameter is fixed by the microwave background observations as it is related with the amplitude of the final curvature power spectrum.

## II. PERFECT FLUID QUANTUM BOUNCE

### A. Single Fluid Bounce

As discussed in the introduction, we assume that the relevant distance scales are sufficiently large during the overall evolution of the universe that one can coarse-grain its matter content distribution and thus approximate its description by means of a perfect fluid, keeping in mind that this hypothesis needs be verified when the relevant parameters are compared with observational data. Assuming natural units ( $\hbar = c = 1$ ) throughout, our classical starting point therefore contains the Einstein-Hilbert GR action  $\mathcal{S}_{\text{HE}}$  together with that describing a perfect fluid  $\mathcal{S}_{\text{fluid}}$ , namely

$$\mathcal{S}_{\text{tot}} = \mathcal{S}_{\text{HE}} + \mathcal{S}_{\text{fluid}} = - \int \sqrt{-g} \left( \frac{R}{6\ell_P^2} + p \right) d^4x, \quad (1)$$

with  $\ell_P = (8\pi G_N/3)^{1/2}$  the Planck length,  $G_N$  the gravitational constant, and  $p$  the fluid pressure, related to its energy density  $\rho$  through  $p = w_r \rho$ ; in the practical application below, we shall set  $w_r \rightarrow \frac{1}{3}$  to describe a radiation-dominated bounce. Note at this point that we are considering only one fluid, as we are interested in describing the quantum-led bounce; other fluids will enter in the classical regime, and we assume their relative contributions to be negligible during the quantum phase.

Restricting attention to the flat metric

$$ds^2 = -N^2(\bar{\tau}) d\bar{\tau}^2 + a^2(\bar{\tau}) \delta_{ij} dx^i dx^j, \quad (2)$$

thereby defining a timelike variable  $\bar{\tau}$  and the scale factor  $a(\bar{\tau})$ . Describing the fluid in terms of velocity potentials, the corresponding Hamiltonian  $H_{\text{tot}}$  resulting from the action (1) reads

$$H_{\text{tot}} \equiv N \left( \frac{P_\tau}{a^{3w_r}} - \frac{\ell_P^2 P_a^2}{4aV_c} \right) \approx 0, \quad (3)$$

the last weak inequality expressing the classical Dirac constraint. In Eq. (3),  $V_c$  is the (finite) comoving volume of the spatial sections (space being assumed compact for subsequent quantization reasons) and  $P_\tau$  the canonical momentum conjugate to a variable  $\tau$  defined by the fluid (to be later identified with the time variable  $\bar{\tau}$ ). The comoving volume  $V_c$  and the Planck length  $\ell_P$  can be pulled out of the system and absorbed in a variable redefinition.

Setting the lapse  $N \rightarrow a^{3w_r}$  in (3) results in a deparametrization of the Hamiltonian  $H_{\text{tot}}$ , whose linear term becomes exactly  $P_\tau$ . The associated fluid variable thus takes the meaning of a time so we can identify  $\bar{\tau} = \tau$  in what follows. Quantizing à la Dirac by substituting  $P_a \rightarrow -i\partial/\partial a$  and  $P_\tau \rightarrow -i\partial/\partial\tau$  (and hence  $H_{\text{tot}} \rightarrow \hat{H}_{\text{tot}}$ ) then transforms the timeless Wheeler DeWitt equation  $\hat{H}_{\text{tot}}\Psi = 0$  into the time-dependent Schrödinger equation

$$i\frac{\partial}{\partial\tau}\Psi = \frac{\ell_p}{4V_c} \left\{ a^{(3w_r-1)/2} \frac{\partial}{\partial a} \left[ a^{(3w_r-1)/2} \frac{\partial}{\partial a} \right] \right\} \Psi, \quad (4)$$

for the wave function  $\Psi(a, \tau)$ , equation in which we chose a specific ordering of the non commuting operators  $a$  and  $p_a$  compatible with covariance. Changing the fundamental variable  $a$  to  $q$  through

$$q = \frac{2\sqrt{V_c}}{3(1-w_r)\ell_p} a^{\frac{3}{2}(1-w_r)} \quad (5)$$

transforms Eq. (4) into the time-reversed free particle Schrödinger equation:<sup>1</sup>

$$i\frac{\partial}{\partial\tau}\Psi(q, \tau) = \frac{1}{4}\frac{\partial^2}{\partial q^2}\Psi(q, \tau). \quad (6)$$

As (6) is restricted to positive values of  $q$ , one needs to impose the relation

$$\left( \Psi^* \frac{\partial\Psi}{\partial q} - \Psi \frac{\partial\Psi^*}{\partial q} \right) \Big|_{q=0} = 0, \quad (7)$$

in order to preserve the Hamiltonian's self-adjointness [19]. This condition is trivially satisfied by the (real) Gaussian state

$$\Psi_{\text{ini}}(q) = \left( \frac{8}{\pi\tau_B} \right)^{1/4} \exp\left(-\frac{q^2}{\tau_B}\right), \quad (8)$$

which we choose as our initial condition. Using the propagator of Eq. (6) then yields the full time-dependent wave function  $\Psi(q, \tau)$ , written in terms of the rescaled scale factor  $\tilde{a}^{\frac{3}{2}(1-w_r)} = \sqrt{V_c}a^{\frac{3}{2}(1-w_r)}/\ell_p$ , namely

$$\Psi(\tilde{a}, \tau) = \left( \frac{8\tau_B/\pi}{\tau^2 + \tau_B^2} \right)^{1/4} \exp\left[ \frac{-4\tau_B\tilde{a}^{3(1-w_r)}}{9(1-w_r)^2(\tau^2 + \tau_B^2)} \right] e^{iS}, \quad (9)$$

the phase  $S(\tilde{a}, \tau)$  being given by

$$S(\tilde{a}, \tau) = \frac{\pi}{4} - \frac{1}{2} \arctan\left(\frac{\tau_B}{\tau}\right) - \frac{4\tau\tilde{a}^{3(1-w_r)}}{9(1-w_r)^2(\tau^2 + \tau_B^2)}. \quad (10)$$

Eq. (9) was first obtained in Ref. [3] in which it appears as Eq. (20), with slightly different notations. Eq. (7), being proportional to the conserved current of the Schrödinger equation, is then satisfied at all times.

There are various ways to obtain a meaningful trajectory out of the wave function. Most are semiclassical (or semiquantum [21]), when the probability density is sufficiently peaked. In a more general situation however, e.g. [22], one may use the formulation of Refs. [23–25] adapted to quantum cosmology [26], specifically based on such trajectories obtained in a quantum equivalent of the eikonal light-ray approximation in electrodynamics [27]. Among the many advantages of such a formulation is the fact that the "quantumness" of the trajectory is easily evaluated by a simple computation of the quantum potential  $Q[\Psi(\tau)]$  acting on the trajectory which can be calculated from the wave function itself: the smaller  $Q$ , the more classical the system.

In the case at hand, the trajectory is obtained by setting the momenta  $P_q = \partial S/\partial q$ , as in the Hamilton-Jacobi theory, but now  $S(q, \tau)$  is the phase of the wave function. The relationship between the momenta and velocities is obtained as usual, with  $\dot{q}$  given by the Poisson bracket with the reduced Hamiltonian stemming from the constraint (3), which, in the classical case, would simply be the partial derivative of this Hamiltonian with respect to  $q$ , i.e. Hamilton equation. In the case of quantum cosmology, we get

$$\frac{d\tilde{a}}{d\tau} = -\frac{\tilde{a}^{3w_r-1}}{2} \frac{\partial S}{\partial \tilde{a}}, \quad (11)$$

where  $\partial S/\partial \tilde{a}$  is given by

$$\frac{\partial S}{\partial \tilde{a}} = -\frac{4\tau\tilde{a}^{2-3w_r}}{3(\tau^2 + \tau_B^2)(1-w_r)}. \quad (12)$$

Substituting (12) in (11) then gives the first order ordinary differential equation

$$\frac{d\tilde{a}}{d\tau} = \frac{2}{3} \frac{\tau\tilde{a}}{(\tau^2 + \tau_B^2)(1-w_r)}, \quad (13)$$

which is readily integrated. Its solution can be put in the form

$$a(\tau) = a_B \left[ 1 + \left( \frac{\tau}{\tau_B} \right)^2 \right]^{\frac{1}{3(1-w_r)}}, \quad (14)$$

where we switched back to  $a$  instead of  $\tilde{a}$  to recover a dimensionless variable. We note that this solution explicitly replaces the singularity by a bounce at  $\tau = 0$ , with minimal value  $a_B$  of the scale factor.

Note that  $\tau$  is related to cosmic time  $t$  through  $dt = a^{3w_r}d\tau$ . One can then calculate the Hubble parameter in terms of the fluid time  $\tau$ , namely

$$H(t) \equiv \frac{1}{a} \frac{da}{dt} = \frac{2\tau a^{-3w_r}}{3(\tau^2 + \tau_B^2)(1-w_r)}, \quad (15)$$

<sup>1</sup> Note that, the scale factor being assumed dimensionless, the variable  $q$  has dimensions given by those of  $\sqrt{V_c}/\ell_p$ , i.e. the square-root of a length.

which, when expressed in terms of the scale factor, reads

$$H = \pm \frac{2}{3(1-w_r)\tau_B} \frac{1}{a_B^{3w_r}} \sqrt{\left(\frac{a_B}{a}\right)^{3(1+w_r)} - \left(\frac{a_B}{a}\right)^6}. \quad (16)$$

The plus and minus signs respectively describe the expanding and contracting phase.

To simplify the expressions that follow, we introduce the variable  $x \equiv a_0/a = 1+z$ , with  $z$  the usual redshift. In terms of  $x$ , the Hubble parameter can be written as

$$H^2 = \frac{4a_0^{-6w_r} x_B^{-3(1-w_r)}}{9(1-w_r)^2 \tau_B^2} \left[ x^{3(1+w_r)} - \frac{x^6}{x_B^{3(1-w_r)}} \right]. \quad (17)$$

At this stage, we restrict attention to a single component, radiation, since it dominates the dynamics in the bounce phase. Other contributions, such as matter, become relevant only on much larger scales and will be taken into account later. Throughout, the index 0 on a time-dependent function denotes its value at a reference time, to be specified below.

Equation (17) is nothing but the usual Friedman equation for a perfect fluid with equation of state  $w_r$ , but with an additional term  $\propto -x^6$ , i.e. the corrected Friedman equation is phenomenologically equivalent to adding an extra stiff “quantum matter” term with negative energy density  $\rho_Q \propto a^{-6}$ . One can thus rewrite the quantum evolution as

$$H^2 = \frac{8\pi G_N}{3} (\rho - \rho_Q), \quad (18)$$

or, setting  $\rho = \Omega_B \rho_{\text{crit}} x^{3(1+w_r)}$ , with  $\Omega_B$  the fraction of energy density compared to the critical density  $\rho_{\text{crit}} \equiv 3H_0^2/(8\pi G_N)$

$$\left(\frac{H}{H_0}\right)^2 = \Omega_B x^{3(1+w_r)} - \Omega_Q x^6, \quad (19)$$

thereby defining  $\Omega_Q$ . A direct comparison between (19) and (17) yields

$$\Omega_B = \frac{4a_0^{-6w_r} x_B^{-3(1-w_r)}}{9H_0^2 (1-w_r)^2 \tau_B^2}, \quad (20a)$$

$$\Omega_Q = \frac{4a_0^{-6w_r} x_B^{-6(1-w_r)}}{9H_0^2 (1-w_r)^2 \tau_B^2} = \frac{\Omega_B}{x_B^{3(1-w_r)}}. \quad (20b)$$

As one can see from Eq. (19), for  $w_r < 1$  the quantum part of this equation becomes negligible for large values of the scale factor  $a$ , and the classical evolution is recovered.

Once the fluid density  $\Omega_B$  is determined, Eq. (20a) gives a relation between  $x_B$  and  $\tau_B$ , which are the only free parameters introduced by the quantum trajectory. Therefore, since the fluid density and  $H_0$  are potentially determined by observational data measured long after the bounce occurred, implementing such a bouncing scenario requires only one new parameter, namely  $x_B$ , i.e. the size of the reference scale factor in units of its minimum bouncing value.

Given the above, one can easily consider extensions to make this quantum bouncing model closer to the actual universe. Consider some other fluid with equation of state less than that of the bounce dominating fluid  $w_r$ . In this case, given a long enough contracting phase, the term  $\propto x^{3(1+w_r)}$  in the Friedman equation dominates over this new fluid throughout the bouncing phase in which the quantum correction may be relevant. Adding this new fluid is therefore irrelevant as far as the effective quantum trajectory is concerned, and one can approximate its contribution to be relevant only during the classical expanding phase.

In modeling the contracting phase, we do not require it to exactly mirror the expanding one. Processes such as particle creation could alter the composition of the universe after the bounce, leading to some differences between the two phases. However, we do not expect a radical change in the overall composition, and some correspondence between the contracting and expanding branches must be established. To make this connection, we introduce the reference scale factor  $a_0$ , defined during the contracting phase as the value for which the comoving Hubble radius equals the present comoving Hubble radius, i.e.  $c/|H(t_{0-})| = c/|H(t_{0+})|$ . For a perfectly symmetric model with the bounce placed at  $t = 0$ , this would imply  $t_{0-} = -t_{0+}$ . In a more general, slightly asymmetric case, these times need not coincide exactly but remain reasonably close, ensuring a consistent matching between contraction and expansion.

## B. Two Fluids with Radiation dominated bounce

In what follows, and according to the discussion of the previous section, we make the assumption that the bounce occurs during the radiation dominated phase ( $w_r = 1/3$  in the previous section), noting that this is the expected behavior in any model containing matter or dark matter, since these fluids inevitably behave as radiation as the universe contracts. We also assume that during the classical evolution at large scales, an almost pressureless fluid, akin to dark matter, becomes dominant. The sequence of events we have in mind begins with a phase of matter domination (the dust contraction in the so-called matter bounce scenario) in which the perturbations we will be interested in are initiated. Then radiation takes over, and the quantum corrections trigger the end of contraction through a smooth bounce, from which point the standard cosmological model ensues. A similar background model, with an exactly pressureless fluid, was solved in Ref. [28].

To describe the bounce with radiation as the dominant component, the Friedmann equation (19) is specialized by setting  $w_r \rightarrow 1/3$  and replacing  $\Omega_B \rightarrow \Omega_r$ , so that the corresponding term becomes  $\Omega_r x^4$ . In this case, the lapse choice made above simplifies to  $N \rightarrow a^{3w_r} = a$ , and the fluid time  $\tau$  coincides with the conformal time,  $\tau = \eta$ .

To ensure consistency with the observed expanding

Universe, we incorporate one additional component, notably a dust contribution modeled as a perfect fluid with a small equation-of-state parameter ( $w \ll 1$ ). We exclude any dark-energy-like component (such as a cosmological constant  $\Lambda$ ) for two reasons: (i) its presence would not qualitatively alter the bounce dynamics (see also Ref. [6] for the case where a dark energy era takes place only at large scales in the expanding phase), and (ii) it would necessitate a redefinition of the perturbation vacuum state, as detailed in Refs. [29, 30]. Consequently, our model explicitly assumes the absence of dark energy during the contracting phase.

In the limit  $w \rightarrow 0$ , the term  $\Omega_w x^{3(1+w)}$  reduces to  $\Omega_m x^3$ . While radiation dominates for  $x \gtrsim \Omega_m/\Omega_r$ , the values of  $\Omega_m$  and  $\Omega_r$  can be chosen such that this transition occurs sufficiently far from the bounce, where the classical approximation remains valid. Thus, our model is phenomenologically described by the following modification of Eq. (18):

$$E^2 = \Omega_r x^4 + \Omega_w x^{3(1+w)} - \Omega_Q x^6,$$

where  $E^2 \equiv H^2/H_0^2$ , and  $E \equiv \sqrt{E^2}$  denotes its positive square root.

The addition of the extra fluid in Eq. (20b) introduces a slight change in our previous discussion, namely that the value  $x_B$  no longer marks the true bounce point since  $E(x_B) \neq 0$ . This is however easily resolved by recalling that  $x_B$  is a free parameter depending on the arbitrary reference scale factor. We can use its normalization freedom to choose  $E(x_B) = 0$ . Doing so fixes the quantum contribution as

$$\Omega_Q = \frac{\Omega_r}{x_B^2} + \frac{\Omega_w}{x_B^{3(1-w)}},$$

yielding a Hubble function of the form

$$E^2 = \Omega_r \left( x^4 - \frac{x^6}{x_B^2} \right) + \Omega_w \left[ x^{3(1+w)} - \frac{x^6}{x_B^{3(1-w)}} \right], \quad (21)$$

which now explicitly satisfies the bounce condition  $E(x_B) = 0$ . Note that this reparametrization preserves late-time cosmology, as it reduces to the classical relation  $E^2 = \Omega_r x^4 + \Omega_w x^{3(1+w)}$  for  $x_B \gg 1$ .

Using the above parametrization in Eq. (20b), we get

$$\frac{x_B^{-4}}{a_0^2 H_0^2 \eta_B^2} = \frac{\Omega_r}{x_B^2} + \frac{\Omega_w}{x_B^{3(1-w)}}, \quad (22)$$

where

$$\eta_B = \frac{R_{H_0}}{a_0 \sqrt{\Omega_r x_B^2 + \Omega_w x_B^{1+3w}}}, \quad (23)$$

in which we defined the Hubble radius today  $R_{H_0} \equiv c/H_0$ . Using  $\Omega_r = 10^{-7}$ , and  $R_{H_0} \approx 4283 \text{ Mpc}$  (with  $H_0 = 70 \text{ km} \cdot \text{s}^{-1} \cdot \text{Mpc}^{-1}$ ), one gets  $\eta_B \approx 4.2 \times$

$10^{29} \text{ m}/(a_0 x_B)$ . At an arbitrary time, the Hubble radius is

$$R_H = \frac{R_{H_0}}{E}. \quad (24)$$

A key point concerns the range of validity of the Wheeler-DeWitt approach used to produce the background bounce. Canonical quantization should only be trusted when the curvature scale at the bounce is well above the Planck length. The curvature radius is proportional to  $a_B \eta_B$ , which from the above expressions gives

$$a_B \eta_B \approx 4.2 \left( \frac{10^{30}}{x_B} \right)^2 \times 10^{-31} \text{ m} \approx 2.6 \left( \frac{10^{30}}{x_B} \right)^2 \times 10^4 \ell_P,$$

Thus, for values around  $x_B \simeq 10^{30}$  the curvature scale at the bounce is many orders of magnitude larger than  $\ell_P$ . This is the regime in which the Wheeler-DeWitt treatment can be expected to give a reliable semiclassical description of the background. The same scale also controls the amplitude of the perturbations, so remaining in the range up to  $x_B \sim 10^{30}$  simultaneously satisfies both requirements.

Unless otherwise stated, throughout this work we adopt the following fiducial cosmology, i.e. we assume a spatially flat background with

$$\begin{aligned} \Omega_r &= 10^{-7}, & \Omega_w &= 1 - \Omega_r, & w &= 10^{-10}, \\ H_0 &= 70 \text{ km} \cdot \text{s}^{-1} \cdot \text{Mpc}^{-1}, & x_B &= 10^{30}. \end{aligned} \quad (25)$$

These parameter choices, in particular the small value of  $w$  and the large  $a_B$ , will be discussed in detail in Sec. III, where their influence on the perturbations and resulting power spectra is analyzed.

### C. Connecting branches

Having described the parametrization of the contracting phase, we now relate those parameters to the quantities used to describe the expanding universe and current observations. Our strategy is to anchor the contracting branch to the expanding one by matching the magnitude of the Hubble parameter. Concretely, we define  $a_0$  on the contracting branch and  $\tilde{a}_0$  on the expanding branch through the condition  $|H(a_0)| = \tilde{H}(\tilde{a}_0) \equiv H_0$ , where  $H_0$  is the present-day Hubble rate. This provides a common reference point without introducing additional arbitrary scales or assuming any dynamical continuity across the bounce.

In practice, we describe both background solutions by expressing the Hubble parameter as a function of the scale factor. Since the scale factor alone does not distinguish between expansion ( $H > 0$ ) and contraction ( $H < 0$ ), we introduce a notational convention: quantities without a tilde refer to the contracting branch, while tilded quantities refer to the expanding one. Accordingly,  $H(a)$  denotes the Hubble function during contraction,

and  $\tilde{H}(a)$  the same function evaluated along the expanding solution.

Both quantities are defined in the standard way as  $\dot{a}/a$ , with the tilde serving only as a bookkeeping device. If one introduces a time coordinate with  $t = 0$  at the bounce, this corresponds to  $H \equiv (\dot{a}/a)|_{t<0}$  and  $\tilde{H} \equiv (\dot{a}/a)|_{t>0}$ .

During the expanding phase, the background evolution is described by

$$\frac{\tilde{H}^2}{H_0^2} = \tilde{\Omega}_r \left( \frac{\tilde{a}_0}{a} \right)^4 + \tilde{\Omega}_w \left( \frac{\tilde{a}_0}{a} \right)^3 + \tilde{\Omega}_b \left( \frac{\tilde{a}_0}{a} \right)^3 + \Omega_\Lambda, \quad (26)$$

where quantities with a tilde refer to the expanding branch, and  $\tilde{\Omega}_b$  and  $\tilde{\Omega}_\Lambda$  denote the present-day baryon density parameter and cosmological constant, respectively. We neglect the small effect of a nonzero equation-of-state parameter  $w$  in the background evolution, i.e. we set  $a^{-3(1+w)} \approx a^{-3}$  since  $w \ll 1$ .

In contrast, during the contracting phase, we consider models without baryons and without a cosmological constant. If the only difference between the two branches were the absence of these components, the corresponding expression would be

$$\frac{H^2}{H_0^2} = \tilde{\Omega}_r \left( \frac{\tilde{a}_0}{a} \right)^4 + \tilde{\Omega}_w \left( \frac{\tilde{a}_0}{a} \right)^3. \quad (27)$$

Evaluating this expression at  $a = a_0$ , where by definition  $|H| = H_0$ , we obtain

$$1 = \tilde{\Omega}_r \left( \frac{\tilde{a}_0}{a_0} \right)^4 + \tilde{\Omega}_w \left( \frac{\tilde{a}_0}{a_0} \right)^3. \quad (28)$$

This equation corresponds to a fourth-order polynomial for  $\tilde{a}_0/a_0$ . Rather than solving it numerically, we exploit the hierarchy  $\tilde{\Omega}_r \ll \tilde{\Omega}_w$  and solve perturbatively in powers of  $\tilde{\Omega}_r$ . This yields

$$\frac{\tilde{a}_0}{a_0} = \frac{1}{\tilde{\Omega}_m^{1/3}} - \frac{\tilde{\Omega}_r}{3\tilde{\Omega}_m^{5/3}} + \frac{\tilde{\Omega}_r^2}{3\tilde{\Omega}_m^3} - \frac{35\tilde{\Omega}_r^3}{81\tilde{\Omega}_m^{13/3}} + \mathcal{O}(\tilde{\Omega}_r^4). \quad (29)$$

Using  $\tilde{T}_\gamma = 2.7245$  K today and  $\tilde{\Omega}_w = 0.25$ , we find  $\tilde{a}_0/a_0 \approx 1.6$ . Thus, the same value of the Hubble parameter occurs at a scale factor slightly smaller than today's value in the expanding universe. If the contracting phase differed from the expanding one only by the absence of baryons and a cosmological constant, the Hubble function during contraction could be written as

$$\frac{H^2}{H_0^2} = \tilde{\Omega}_r \left( \frac{\tilde{a}_0}{a_0} \right)^4 x^4 + \tilde{\Omega}_w \left( \frac{\tilde{a}_0}{a_0} \right)^3 x^3, \quad (30)$$

which implies the identifications

$$\Omega_r = \tilde{\Omega}_r \left( \frac{\tilde{a}_0}{a_0} \right)^4, \quad \text{and} \quad \Omega_w = \tilde{\Omega}_w \left( \frac{\tilde{a}_0}{a_0} \right)^3. \quad (31)$$

These identifications hold only under the assumption stated above, namely that the contracting phase differs

from the expanding one solely by the absence of baryons and a cosmological constant. In this symmetric situation, the radiation content of the contracting branch is completely fixed by a backward extrapolation of present-day expanding-phase quantities.

We now relax the symmetric assumption discussed above and allow for more asymmetric scenarios. In particular, the radiation temperature during contraction need not be fixed by its expanding-phase value. Moreover, since the density parameters satisfy  $\sum \Omega_i = 1$  independently in each branch, specifying the radiation content during contraction fully determines the background evolution in that phase. Using the standard relation  $\Omega_r \propto T_\gamma^4$ , evaluated separately in each branch, we therefore introduce the asymmetry parameter

$$\gamma_{\text{assym}} \equiv \frac{T_\gamma}{\tilde{T}_\gamma(\tilde{a}_0/a_0)} = \left( \frac{\Omega_r}{\tilde{\Omega}_r} \right)^{1/4} \left( \frac{a_0}{\tilde{a}_0} \right), \quad (32)$$

which quantifies deviations from a symmetric matching between the contracting and expanding branches. The parameter  $\gamma_{\text{assym}}$  measures the mismatch between the radiation temperature inherited by the contracting branch and the value obtained by a symmetric extrapolation of today's CMB temperature back to  $a = a_0$ , with  $\gamma_{\text{assym}} = 1$  corresponding to a perfectly symmetric matching, for which Eq. (31) is recovered. For reference, the fiducial parameters adopted in Eq. (25) correspond to  $\gamma_{\text{assym}} \simeq 0.13$  (using  $\tilde{T}_\gamma$  and  $\tilde{\Omega}_w$  as above).

Such an asymmetry is generic in bouncing cosmologies. Entropy production, particle creation, or incomplete thermalization across the bounce can modify the radiation content between contraction and expansion, even when the large-scale background dynamics remain smooth. The parameter  $\gamma_{\text{assym}}$  provides a simple and model-independent way of capturing these effects at the background level, without committing to a specific microphysical realization of the bounce.

### III. PERTURBATIONS IN A CONTRACTING UNIVERSE

Our primary goal is to connect primordial perturbations to observable signatures in the cosmic microwave background (CMB). To achieve this, we compute the power spectrum of comoving modes  $k_c$  that seed CMB temperature anisotropies. Recall that we defined  $a_0$  as the scale factor at which the Hubble radius matches its current value; at this epoch, the corresponding physical wavenumbers are  $k = k_c/a_0$ . While CMB observations constrain modes in the range  $10^{-6} \text{ Mpc}^{-1} \lesssim k \lesssim 1 \text{ Mpc}^{-1}$ , we extend our analysis to  $10^{-8} \text{ Mpc}^{-1} \lesssim k \lesssim 10^8 \text{ Mpc}^{-1}$  to account for potential differences between contracting and expanding phases and to encompass smaller-scale modes that may become observable in the future.

In this section, we recall the quantum cosmological perturbations of a two fluid system [17]. For the fluids part,

we follow Ref. [31] and apply the variational formalism for perfect fluids proposed in Ref. [32]. Our action is therefore chosen to be

$$\mathcal{S} = \int \left( \frac{R}{6\ell_p^2} + p_w + p_r \right) \sqrt{-g} d^4x, \quad (33)$$

where  $p_w$  and  $p_r$  respectively refer to the pressures of the almost pressureless fluid and the radiation fluid leading to the bounce of Sec. II. We now specialize in the case of small perturbations evolving on the flat and regular FLRW metric introduced in the previous section. We choose comoving coordinates normalized at  $a_0$ , the scale factor at which the Hubble radius takes its present value. With this choice, the determinant of the metric becomes  $\sqrt{-g} = (a/a_0)^3$ , rather than  $a^3$  as used in [17].

### A. Notations and relevant variables

The scalar sector is sufficient to capture the physical degrees of freedom relevant to the dynamics considered here, while vector and tensor modes can be treated independently. Following the standard decomposition, we write the perturbed metric as

$$ds^2 = -(1 - 2\phi)N^2 d\bar{\tau}^2 - N\partial_i \mathcal{B} dx^i d\bar{\tau} + [a^2 \delta_{ij} (1 + 2\psi) - 2\partial_i \partial_j \mathcal{E}] dx^i dx^j, \quad (34)$$

where  $\phi$ ,  $\mathcal{B}$ ,  $\psi$ , and  $\mathcal{E}$  represent the scalar perturbations of the lapse, shift, and spatial metric, respectively. The perturbations of the energy-momentum tensor are written similarly

$$T_0^0 = -\delta\rho, \quad (35a)$$

$$T_i^0 = N^{-1}(\rho + p)\partial_i \mathcal{V}, \quad (35b)$$

$$T_i^j = \delta\rho\delta_i^j = c_i^2 \delta\rho\delta_i^j, \quad (35c)$$

where each fluid component carries its own scalar perturbations ( $\delta\rho$ ,  $\mathcal{V}$ ) and speed of sound  $c_i$ , and we are considering only barotropic fluids with no internal entropy perturbation.

The variables  $\phi$  and  $\mathcal{B}$  enter the Lagrangian without time derivatives and therefore act as Lagrange multipliers enforcing the Hamiltonian and momentum constraints. Once these constraints are reduced, the remaining degrees of freedom can be expressed in terms of gauge-invariant combinations of the variables above, which we define below.

Before analyzing the evolution of perturbations, it is useful to identify and define the background quantities that most directly enter the perturbation equations. These quantities also control the validity of adiabatic approximations and determine the relevant time scales in the system.

In the action, described in detail in Ref. [17], one can observe that many terms can be expressed using the combination

$$\gamma_i \equiv \ell_p^2 \frac{a^3(\rho_i + p_i)}{a_0^3 |H|} = \frac{(1 + w_i)\Omega_i}{R_{H_0}} \frac{x^{3w_i}}{E}, \quad (36)$$

where  $i$  denotes the fluid index ( $w$  or  $r$ ). This combination appears repeatedly in the equations of motion and in the expression of the canonical variables, particularly in the adiabatic vacuum construction. We therefore define  $\gamma_i$  as the *gravitational weight* of fluid  $i$ , and also introduce the total gravitational weight  $\gamma = \gamma_w + \gamma_r$ . Rewriting the perturbation equations in terms of  $\gamma_i$  and  $\gamma$  simplifies the formalism and highlights the contribution of each fluid component to the dynamics.

In addition to the gravitational weights, the sound speeds  $c_i$  of each fluid are relevant background quantities. Since we consider barotropic fluids with constant equations of state, the individual sound speeds are given by  $c_w = \sqrt{w}$  and  $c_r = 1/\sqrt{3}$ . However, the propagation of perturbations is governed not only by these values but also by their combinations. The frequencies of the curvature and isocurvature modes are determined by the effective curvature ( $c_\zeta$ ) and isocurvature ( $c_Q$ ) sound speeds, respectively given by

$$c_\zeta^2 \equiv \frac{\gamma_w c_w^2 + \gamma_r c_r^2}{\gamma}, \quad (37)$$

$$c_Q^2 \equiv \frac{\gamma_w c_r^2 + \gamma_r c_w^2}{\gamma}. \quad (38)$$

A key dimensionless quantity in the mode equations is the Hubble-scaled wavenumber, defined as the ratio of the physical wavenumber ( $k_c/a$ ) to the Hubble rate  $|H|$

$$F_\nu \equiv \frac{k_c}{a|H|} = kxR_H, \quad (39)$$

where  $k \equiv k_c/a_0$  is the physical wavenumber (equivalently,  $\lambda \equiv 1/k$  is the reduced wavelength) at the present time. Note that  $kx$  is the wavenumber rescaled to the scale factor  $a$ , and  $R_H$  is the Hubble radius at  $a$ . Moreover, although  $F_\nu$  does not depend on the fluid type, it does however depend on the scale factor  $x$  in the same way as the gravitational weight  $\gamma_r$ .

For each fluid component, one can define a gauge-invariant curvature perturbation, denoted by  $\zeta_w$  and  $\zeta_r$ , respectively, for the matter and radiation fluids (see, e.g., Ref. [33]; they correspond to the fluid velocity perturbations  $\mathcal{U}$  in Ref. [17]). These quantities can be combined into a total curvature perturbation  $\zeta$ , defined by the weighted sum

$$\zeta = \frac{\gamma_w \zeta_w + \gamma_r \zeta_r}{\gamma}, \quad (40)$$

the gravitational weights  $\gamma_i$  being defined in (36). The conjugate momentum associated with  $\zeta$  involves the gauge-invariant energy density contrasts of each fluid, given by

$$\bar{\delta}_{\rho_i} \equiv \frac{\delta\rho_i}{\rho_i + p_i} + 3\psi, \quad (41)$$

where  $\psi$  is the metric perturbation defined in Eq. (34). The total energy density contrast is then expressed as

$$\bar{\delta}_\rho = \frac{\gamma_w \bar{\delta}_{\rho_w} + \gamma_r \bar{\delta}_{\rho_r}}{\gamma}, \quad (42)$$

and the corresponding conjugate momentum for the curvature perturbation is

$$\Pi_\zeta = s\gamma(3\zeta - \bar{\delta}_\rho), \quad (43)$$

where  $s = H/|H|$  denotes the sign of the Hubble parameter, i.e.  $s = -1$  in the contracting phase and  $s = +1$  during expansion. This definition of  $\Pi_\zeta$  combines the total energy density fluctuation ( $\bar{\delta}_\rho$ ) with the spatial curvature ( $\zeta$ ). Consequently,  $\Pi_\zeta$  is dynamically sensitive only to genuine curvature perturbations and remains unaffected by pure isocurvature (entropy) modes.

As shown in Ref. [17], see Eq. (33) for a flat background, the curvature perturbation for each fluid reads  $\zeta_i = \psi + H\mathcal{V}_i$ , where  $\mathcal{V}_i$  is the (gauge-dependent) velocity potential associated with fluid  $i$  and  $\psi$  the (gauge-dependent) curvature perturbation. In the constant-curvature gauge ( $\psi = 0$ ), this relation reduces to  $\zeta_i = H\mathcal{V}_i$ , showing that  $\zeta_i$  differs from the velocity potential by an extra factor of  $H$ . The physical velocity perturbation is given by the spatial gradient of  $\mathcal{V}_i$ . Motivated by this, we introduce the gauge-invariant variable

$$F_\nu \zeta_i \xrightarrow{\psi \rightarrow 0} kx \mathcal{V}_i, \quad (44)$$

which, in the constant-curvature gauge, coincides with the modulus of the gauge-dependent velocity perturbation. Note that in this gauge, the gauge-invariant contrast  $\bar{\delta}_{\rho_i}$  reduces to the gauge-dependent energy density contrast  $\propto \delta\rho_i$ .

Although the weighted sum (40) gives the total curvature perturbation, the difference  $\zeta_w - \zeta_r$  provides the so-called isocurvature mode. Explicitly, this is [17]

$$Q = s \frac{\gamma_w \gamma_r}{\gamma} \Delta\zeta, \quad \Delta\zeta \equiv \zeta_r - \zeta_w, \quad (45)$$

with momentum

$$\Pi_Q = \bar{\delta}_{\rho_w} - \bar{\delta}_{\rho_r}, \quad (46)$$

which is the usual definition for isocurvature perturbation between two fluids.

In this work, the term ‘‘adiabatic’’ is used specifically in its WKB or dynamical sense, denoting modes whose amplitude evolves slowly compared to their oscillation period. This is distinct from its other common meaning in cosmology, which describes a compositional perturbation where the relative number densities of species remain unperturbed. To avoid conflating these two concepts, we classify perturbations composition as either curvature (described by  $\zeta$  and  $\Pi_\zeta$ ) or isocurvature (described by  $Q$  and  $\Pi_Q$ ). In multi-fluid systems, the curvature perturbation is sourced not only by the total energy density contrast but also by the collective fluid velocity potential. Consequently, isocurvature perturbations can manifest in two distinct forms: as differences in energy density between fluids (energy isocurvature  $\Pi_Q$ ) or as differences in their velocity potentials (velocity isocurvature  $\Delta\zeta$ ).

In terms of the previously defined variables, the Hamiltonian for scalar perturbations in the two-fluid system, written in Fourier space as  $\delta\mathcal{H}^{(2,s)} = \sum_k \delta\mathcal{H}_k^{(2,s)}$ , is given for each mode  $k$  by

$$\begin{aligned} \ell_p^2 \frac{\delta\mathcal{H}_k^{(2,s)}}{N|H|} = & \frac{c_\zeta^2}{2\gamma} \Pi_{\zeta k}^2 + \frac{\gamma_w \gamma_r c_Q^2}{2\gamma} \Pi_{Q k}^2 \\ & + s \frac{(c_r^2 - c_w^2) \gamma_r \gamma_w}{\gamma^2} \Pi_{\zeta k} \Pi_{Q k} \\ & + \frac{\gamma F_\nu^2}{2} \zeta_k^2 + \frac{\gamma F_\nu^2}{2\gamma_r \gamma_w} Q_k^2, \end{aligned} \quad (47)$$

where  $N$  is the lapse function, whose choice will be specified below.

Our conventions for the momentum  $\Pi_\zeta$  and the variable  $Q$  are related to those in Ref. [17] by the rescaling

$$\Pi_\zeta = \ell_p^2 \Pi_\zeta^{[17]} \quad Q = \ell_p^2 Q^{[17]},$$

all other perturbation variables being left unchanged. Combined with our definition of  $\gamma$ , this ensures all quantities are either dimensionless or carry dimensions of length, even when  $\hbar = c = 1$  is not imposed, which simplifies the Fourier-space analysis. This convention introduced an overall factor of  $\ell_p^2$  in the Hamiltonian above, a factor that can be absorbed through a subsequent rescaling of all perturbation variables. This rescaling is often adopted to normalize the perturbation variables to unity and to simplify numerical computations. Whenever required, we restore the factor by multiplying the perturbation amplitudes by  $\ell_p$ .

The two-fluid Hamiltonian in Eq. (47) yields the following Hamilton equations

$$\frac{1}{N|H|} \frac{d\zeta_k}{d\bar{\tau}} = \frac{c_\zeta^2}{\gamma} \Pi_{\zeta k} + s \Delta c^2 \frac{\gamma_r \gamma_w}{\gamma^2} \Pi_{Q k}, \quad (48a)$$

$$\frac{1}{N|H|} \frac{dQ_k}{d\bar{\tau}} = \frac{\gamma_w \gamma_r c_Q^2}{\gamma} \Pi_{Q k} + s \Delta c^2 \frac{\gamma_r \gamma_w}{\gamma^2} \Pi_{\zeta k}, \quad (48b)$$

$$\frac{1}{N|H|} \frac{d\Pi_{\zeta k}}{d\bar{\tau}} = -\gamma F_\nu^2 \zeta_k, \quad (48c)$$

$$\frac{1}{N|H|} \frac{d\Pi_{Q k}}{d\bar{\tau}} = -\frac{\gamma F_\nu^2}{\gamma_r \gamma_w} Q_k, \quad (48d)$$

with  $\bar{\tau}$  the time coordinate in the perturbed metric (34), defined by the lapse function  $N$ , and we have set  $\Delta c^2 = c_r^2 - c_w^2$ . The solutions to Eqs. (48) will be analyzed below, using vacuum initial conditions specified in the next section. Before addressing these initial conditions, we derive a few relevant quantities from the dynamical system that help the physical interpretation of the perturbation modes, but first we make use of our freedom to choose whatever time gauge we deem suitable to further simplify the Hamilton equations (48). In particular, we emphasize that Eqs. (48) contain the combination  $N|H|$ , suggesting that a time variable absorbing this factor would be advantageous.

Since we consider an evolution through a full phase of cosmological contraction, with the scale factor varying over many orders of magnitude, our choice of time coordinate should reflect this behavior. A natural choice is a logarithmic time variable, which we denote by  $\alpha$ , defined through

$$x = x_B \exp(-|\alpha|), \quad (49)$$

where the bounce occurs at  $\alpha = 0$ , with  $\alpha < 0$  during contraction and  $\alpha > 0$  during expansion. With this choice, the lapse function becomes

$$N = \frac{1}{|H|}, \quad (50)$$

as required. This expression appears ill-defined at the bounce ( $H = 0$ ), so one might ask whether such a time variable is well defined close to the bounce and if one should switch to a different time gauge in the vicinity of the bounce. However, a local analysis of Eq. (21) shows that  $H \propto \pm\sqrt{|\alpha|}$  close to  $\alpha = 0$ , thereby ensuring that the relevant integrals involving  $N$  remain finite;<sup>2</sup> the time gauge  $\alpha$  is regular. From this point on, we therefore set  $N = 1/|H|$ , and denote by a dot a time derivative with respect to the logarithmic time variable  $\alpha$ .

The time evolution of perturbations depends on the gravitational weights  $\gamma_r$  and  $\gamma_w$ , which set the relative contributions of radiation and matter. The ratio  $\gamma_w/\gamma_r$  tracks the transition from radiation to matter dominance, while the combination  $c_i F_\nu$  determines when each mode enters the WKB regime as we will discuss in the next section. These quantities remain central in the adiabatic limit, where derivatives of the background are small, and demonstrate that the coupling between the two fluids is an intrinsic feature of the system rather than a negligible factor. In Fig. 1, we show the evolution of  $\gamma_r$ ,  $\gamma_w$ , and  $F_\nu$ . All quantities display simple power-law behavior during the respective domination phases, with a smooth transition around the matter-radiation equality.

Returning to Hamilton equations (48), we identify two main challenges in solving the system. First, the curvature mode  $\zeta_k$  and the entropy mode  $Q_k$  are dynamically coupled. Second, the coefficients in the equations are time-dependent, reflecting the evolution of the background. As shown in Ref. [17], at early times in the contracting phase the system evolves adiabatically: the characteristic frequencies of the perturbations are much larger than the rates of change of the background quantities, such as  $\gamma_i$  and  $F_\nu$ .

If the coefficients of the system were constant, an exact diagonalization would reduce it to independent harmonic oscillators. With time-dependent coefficients, exact diagonalization is not possible, but we can still perform an

instantaneous diagonalization, separating fast and slow degrees of freedom at each time. This introduces extra terms proportional to time derivatives of the background-dependent coefficients, which are subdominant in the adiabatic regime. The derivation of the adiabatic solution is given in Appendix A.

The analysis reveals two independent degrees of freedom in the system, each associated with a distinct set of basis functions, respectively called Mode 1, propagating at the radiation sound speed  $c_r$ , and Mode 2, propagating at the matter sound speed  $c_w$ . Each set is a nontrivial combination of the two fluid components and cannot be identified solely with either pure curvature or pure isocurvature perturbations. In the initial quantum regime, these mode function sets define the corresponding creation and annihilation operators, ensuring statistical independence. In the classical regime, their variances correspond to statistical (non-quantum) fluctuations. In the WKB analysis, each set evolves according to its characteristic sound speed, reflecting the independent dynamics of the two modes.

To avoid confusion with the underlying fluid components, we adopt the labels Mode 1 and Mode 2 defined above. This prevents ambiguous notation such as  $\zeta_i$ , which could ambiguously refer either to a radiation perturbation or to the total curvature perturbation in Mode 1's basis functions. In practice, we denote these cases as  $\zeta_{r1}$  (radiation curvature perturbation in Mode 1) or  $\zeta_1$  (total curvature perturbation in Mode 1) respectively.

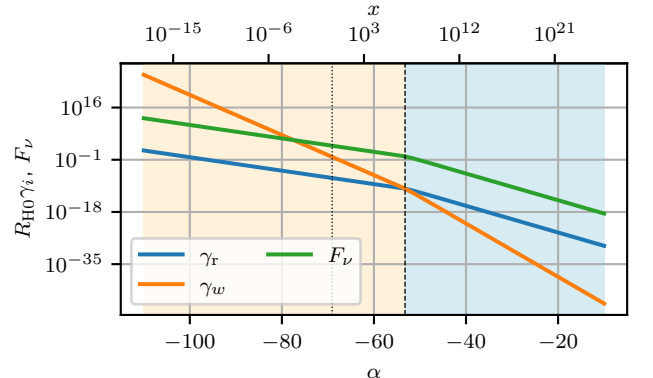


Figure 1. Evolution of the gravitational weights  $R_{H0}\gamma_r$  (blue) and  $R_{H0}\gamma_w$  (orange) as functions of the logarithmic time variable  $\alpha$  (49). The top axis shows the corresponding scale factor  $x = a_0/a$ . The green curve plots the Hubble-scaled wavenumber  $F_\nu$  (39) for  $k = 1 \text{ Mpc}^{-1}$ , using the fiducial cosmology of Eq. (25). Shaded regions mark the radiation-dominated (light blue) and matter-dominated (light orange) eras. Vertical lines indicate key transitions: the matter-radiation equality (dashed) and the epoch when the Hubble radius matches its present value,  $x = 1$  (dotted). As anticipated from Eq. (39),  $F_\nu$  and  $\gamma_r$  exhibit identical time dependence up to a constant factor.

<sup>2</sup> Near  $\alpha = 0$ , one has  $H \propto \pm\sqrt{|\alpha|}$ , so  $t = \int N d\alpha = \int d\alpha/H \propto \pm\sqrt{|\alpha|}$ ; the negative branch applies for  $\alpha < 0$ .

## B. Power Spectra and Correlations

The statistical properties of our perturbation modes are fully characterized by two types of correlation functions: the auto-correlations (power spectra) of individual fields and their cross-correlations. For the curvature perturbation  $\zeta$ , isocurvature perturbation  $\Delta\zeta$ , and energy density contrasts, these correlations contain more information about early universe dynamics.

Building on the mode decomposition, we compute both types of correlations under the vacuum state assumption from Appendix A. The statistical independence of Modes 1 and 2 implies that all correlations decompose additively:

$$\mathcal{P}_X(k) = \mathcal{P}_{X1}(k) + \mathcal{P}_{X2}(k), \quad (51a)$$

$$\mathcal{P}_{XY}(k) = \mathcal{P}_{XY1}(k) + \mathcal{P}_{XY2}(k), \quad (51b)$$

where for each mode  $i = 1, 2$  we define: The *auto-power spectrum* ( $X = Y$ ):

$$\mathcal{P}_{Xi}(k) = \frac{k^3}{2\pi^2} |X_i(k)|^2. \quad (52)$$

The *cross-power spectrum* ( $X \neq Y$ ):

$$\mathcal{P}_{XYi}(k) = \frac{k^3}{2\pi^2} \Re [X_i(k)Y_i^*(k)] \quad (53)$$

The auto-power spectra (e.g.,  $\mathcal{P}_\zeta$ ) characterize field covariances, while the cross-spectra (e.g.,  $\mathcal{P}_{\zeta\Delta\zeta}$ ) reveal correlations between different perturbation types. The  $k^3/(2\pi^2)$  normalization ensures these dimensionless quantities properly represent fluctuation power per logarithmic  $k$ -interval, matching CMB analysis conventions.

## C. Sub Sound-Hubble-Scale Regime

For Mode 1, the adiabaticity is controlled by the radiation Sound-Hubble-Scale (SHS)  $c_{rx}R_H$ , while for Mode 2 it is controlled by the matter SHS  $c_{wx}R_H$ . This naturally divides the time evolution into two separate regimes: super-SHS ( $c_i k x R_H \ll 1$ ) and sub-SHS ( $c_i k x R_H \gg 1$ ), each corresponding to the characteristic SHS of the respective mode.

In Appendix A, we derive the first-order adiabatic corrections to the mode functions, Eqs. (A23) and (A24). Our numerical implementation also includes the second-order corrections, which allow us to define the WKB scale in Eq. (A25) as an estimate of the truncation error of the adiabatic approximation. While the exact expressions are complicated, they are well approximated by the simple quantity  $1/(c_i F_\nu)$ . To illustrate this, Fig. 2 shows the WKB scale for each component multiplied by  $c_i F_\nu$ , demonstrating that this approximation is close to unity, varying only around the matter-radiation transition, but remaining close to unity throughout the rest of the evolution. The two exceptions are the entropy mode

$Q_1$  and its conjugate momentum  $\Pi_{Q1}$ , which rise from near zero to unity around the matter-radiation transition, their smaller values during the matter dominated phase indicate that their adiabatic corrections are even smaller than those of the other components. Since we need all components to be in the WKB regime to have a well-defined approximation and the other components follow  $c_i F_\nu$ , this indicate the latter is still a good proxy for the truncation error of the adiabatic approximation.

The system (48) is coupled. This occurs because, even if the fluids are non-interacting at the background level, their perturbations are coupled through gravity, leading to the momentum-momentum coupling in Eq. (47).<sup>3</sup> Since we assume that cosmological perturbations originate from quantum vacuum fluctuations in the asymptotic past of the background model, where the geometry is nearly flat, an appropriate vacuum state must be defined in this coupled setting. While vacuum state prescriptions (e.g. adiabatic vacua) are well established for free fields, they are less developed for interacting fields. One must therefore employ more general quantization techniques that reduce to the usual adiabatic construction in the free-field limit, but remain valid for systems like (48).

To address this, in Appendix A we construct initial conditions by defining a vacuum state for perturbations in the contracting phase, along the lines of Ref. [17]. There, the generalization of the adiabatic vacuum to the case of  $N$  interacting fluids was first proposed. For clarity, in the present work we rederive the construction explicitly for the two-fluid system, diagonalizing the Hamiltonian (47) in the adiabatic limit and then building the corresponding adiabatic vacuum in the diagonal basis. This procedure yields a consistent choice of initial state that extends the standard adiabatic vacuum to coupled systems, and, to the best of our knowledge, provides a unique treatment in the literature.

## D. Super Sound-Hubble-Scale Evolution

In the super-SHS regime, we expand the Hamilton equations (48) in powers of  $k$ . From Eqs. (48c) and (48d), we see that the leading-order contributions correspond to constant  $\Pi_\zeta$  and  $\Pi_Q$ . Consequently, the solutions for  $\zeta$  and  $Q$  are obtained by integrating these coefficients. These integrals with  $n$  indices  $i_1, \dots, i_n$ , can be written compactly as

$$\mathcal{I}_{i_1 \dots i_n} = \int_{\alpha_1}^{\alpha} d\alpha' \frac{\gamma_{i_1}(\alpha') \dots \gamma_{i_n}(\alpha')}{\gamma^2(\alpha')}, \quad (54)$$

where  $\alpha_1$  is an arbitrary initial time. Using these integrals, the leading-order evolution of  $\zeta$  and  $Q$  in the super

<sup>3</sup> Here only scalars couple to scalars due to the standard scalar-vector-tensor decomposition.

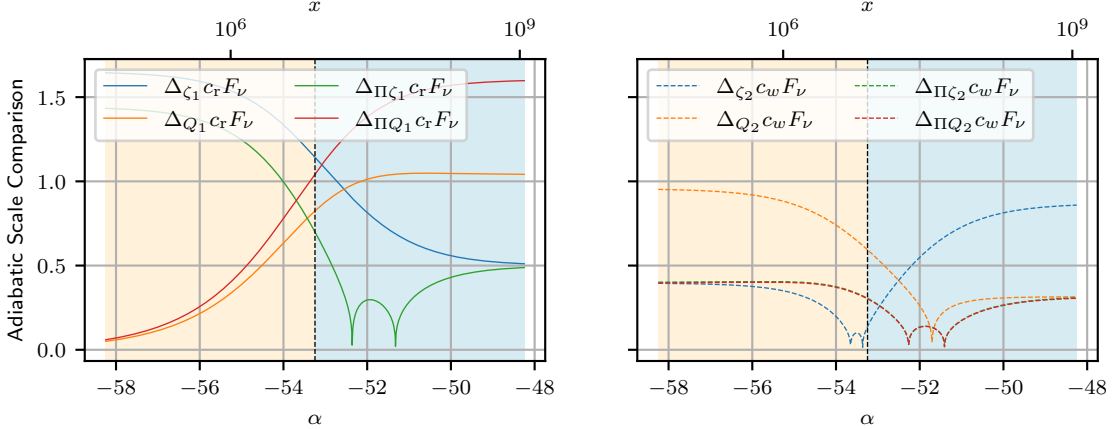


Figure 2. WKB scales  $\Delta_{X_i}$  of Eq. (A25) for each component (Mode 1 left panel, Mode 2 right panel), multiplied by  $c_i F_\nu$ , as a function of the logarithmic time variable  $\alpha$  defined by Eq. (49) during the contraction epoch. The upper axis shows the corresponding scale factor  $x = a_0/a$ . Solid lines correspond to Mode 1 and dashed lines to Mode 2. Blue denotes  $\zeta$ , orange denotes  $Q$ , and green denotes the conjugate momenta  $\Pi_\zeta$  and  $\Pi_Q$ . Shaded regions indicate the radiation-dominated (light blue) and matter-dominated (light orange) domains. The vertical dashed line marks the matter-radiation transition. Most ratios remain close to unity, except for  $Q_1$  and  $\Pi_{Q1}$ , which rise from near zero to unity around the matter-radiation transition. The approach to unity indicates the regime where the simpler  $c_i F_\nu$  correctly approximates the error.

sound-Hubble regime can be expressed as

$$\begin{aligned} \zeta(\alpha) &= \zeta(\alpha_1) \\ &+ c_r^2 [\Pi_\zeta(\alpha_1) \mathcal{I}_r + \Pi_Q(\alpha_1) s \mathcal{I}_{rw}] \\ &+ c_w^2 [\Pi_\zeta(\alpha_1) \mathcal{I}_w - \Pi_Q(\alpha_1) s \mathcal{I}_{rw}], \end{aligned} \quad (55a)$$

$$\begin{aligned} Q(\alpha) &= Q(\alpha_1) \\ &+ c_r^2 [\Pi_Q(\alpha_1) \mathcal{I}_{rw} + \Pi_\zeta(\alpha_1) s \mathcal{I}_{rw}] \\ &+ c_w^2 [\Pi_Q(\alpha_1) \mathcal{I}_{rw} - \Pi_\zeta(\alpha_1) s \mathcal{I}_{rw}], \end{aligned} \quad (55b)$$

These expressions make explicit how the initial momenta,  $\Pi_\zeta(\alpha_1)$  and  $\Pi_Q(\alpha_1)$ , control the leading-order growth of the perturbations. Each term corresponds to contributions from the radiation and matter components, weighted by their respective sound speeds and integrals of the Hamiltonian coefficients.

Now, since the solution derived above is valid only for  $F_\nu < 1$ , we match it to the WKB solution at the transition point  $c_i F_\nu = 1$ , with  $i = r$  for Mode 1 and  $i = w$  for Mode 2. This matching slightly extrapolates the approximate solutions but is sufficient to capture the adiabatic behavior of the perturbations and to connect smoothly with the super sound-Hubble regime. The end condition for the sub sound-Hubble solution is therefore

$$c_i F_\nu = 1, \quad \rightarrow \quad k = \frac{1}{c_i x_i^\times(k) R_H [x_i^\times(k)]}, \quad (56)$$

which implicitly defines the end time  $x_i^\times(k)$  for each wavenumber  $k$ .

If this condition occurs deep in the matter-dominated phase, the end time can be approximated by

$$x_i^\times(k) \approx \left( \frac{c_i R_{H_0} k}{\sqrt{\Omega_w}} \right)^{2/(1+3w)}. \quad (57)$$

At the same epoch the background functions reduce to

$$F_\nu \approx \frac{R_{H_0} k}{\sqrt{\Omega_w}} \frac{1}{x^{(1+3w)/2}}, \quad (58)$$

$$\gamma_w \approx \frac{(1+w)\sqrt{\Omega_w}}{R_{H_0}} \frac{1}{x^{3(1-w)/2}}, \quad (59)$$

$$\gamma_r \approx \frac{4\Omega_r}{3R_{H_0}\sqrt{\Omega_w}} \frac{1}{x^{(1+3w)/2}}. \quad (60)$$

Inserting these expressions into the leading-order WKB solutions (A9)–(A10), we find

$$\bar{\Pi}_{\zeta 1} = is \sqrt{\frac{\gamma_r F_\nu}{2c_r}} \approx is \sqrt{\frac{2\Omega_r}{3\Omega_w c_r}} \frac{k}{x^{(1+3w)}}, \quad (61)$$

$$\bar{\Pi}_{\zeta 2} = -is \sqrt{\frac{\gamma_w F_\nu}{2c_w}} \approx -is \sqrt{\frac{(1+w)}{2c_w}} \frac{k}{x^2}. \quad (62)$$

Evaluating these at the end of the sub-SHS regime gives

$$\bar{\Pi}_{\zeta 1}^\times \approx is \sqrt{\frac{2\Omega_r}{3c_r^3 R_{H_0}} \frac{(R_{H_0} k)^2}{(R_{H_0} k)^3}}, \quad (63a)$$

$$\bar{\Pi}_{\zeta 2}^\times \approx -is \sqrt{\frac{(1+w)}{2c_w R_{H_0}} \left( \frac{\Omega_w}{c_w^2} \right)^{\frac{2}{1+3w}} \frac{(R_{H_0} k)^{\frac{12w}{1+3w}}}{(R_{H_0} k)^3}}, \quad (63b)$$

where superscript  $\times$  indicates the value at the end of the appropriate sub-SHS crossing time, e.g.,  $\bar{\Pi}_{\zeta 1}^\times \equiv \bar{\Pi}_{\zeta 1}[x_r^\times(k)]$  and  $\bar{\Pi}_{\zeta 2}^\times \equiv \bar{\Pi}_{\zeta 2}[x_w^\times(k)]$ . The corresponding

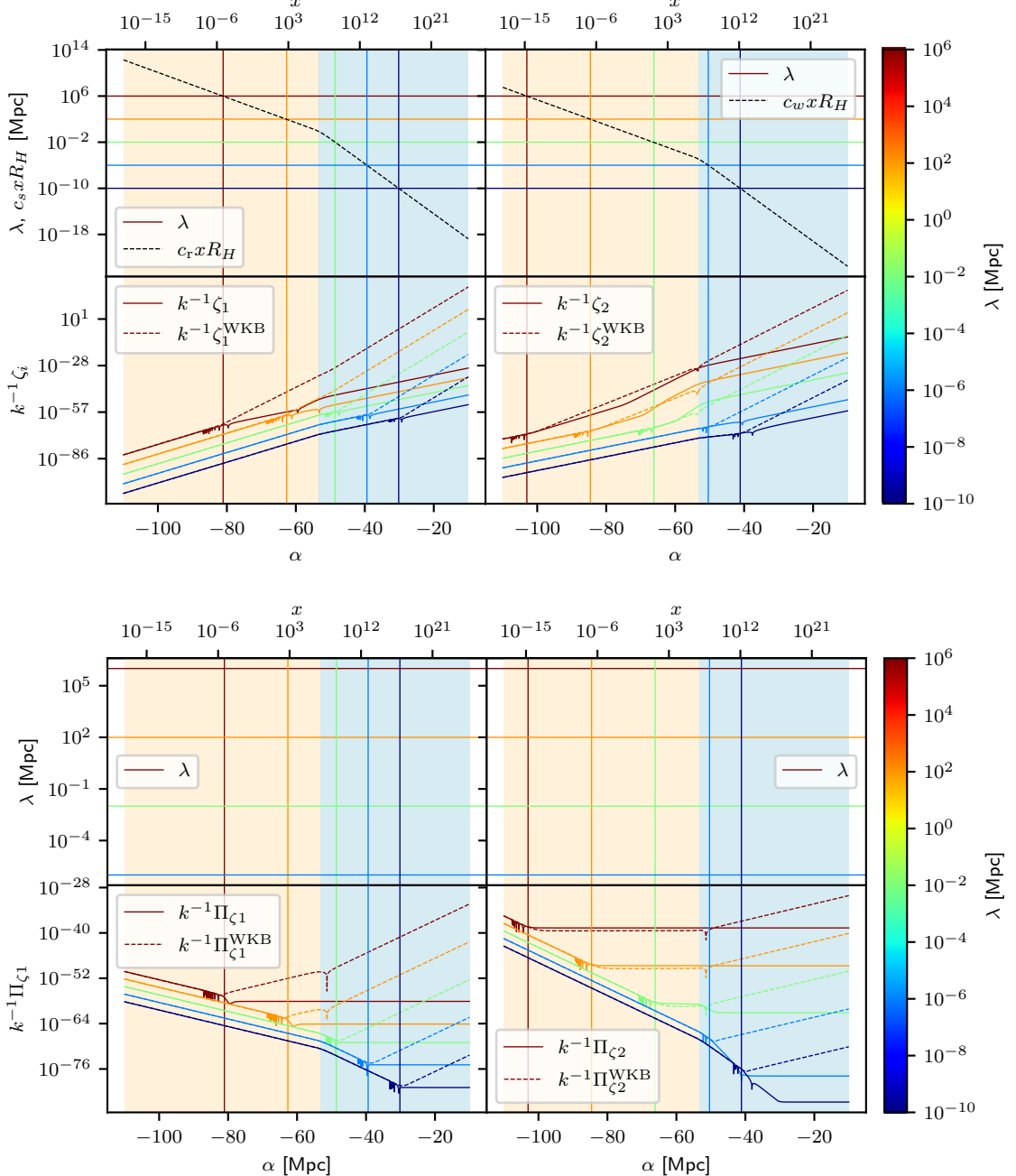


Figure 3. Evolution of multiple modes, each shown in a distinct color with comoving wavelength  $\lambda$  indicated in the color bar (in Mpc). In both figures, the top panels show  $\lambda$  for each mode compared with the comoving Hubble radius multiplied by the relevant sound speed:  $c_i F_\nu/k = c_i x R_H$  for Mode 1 (radiation SHS) on the left, and  $c_w x R_H$  for Mode 2 (matter SHS) on the right. The additional factor  $k^{-1}$  separates the modes visually. The bottom panels in both figures show the evolution of the corresponding perturbation:  $\zeta_1$  and  $\zeta_2$  in the top figure, and  $\Pi_{\zeta 1}$  and  $\Pi_{\zeta 2}$  in the bottom figure. Vertical lines mark the times when  $\lambda = c_i x R_H$ , corresponding to sound-Hubble crossing ( $c_i F_\nu = 1$ ), and help to identify the transition between sub- and super-Hubble behavior for each mode. To emphasize oscillations inside the Hubble radius (sub-Hubble regime), only the real part of the mode functions is plotted. In addition, we also plotted the WKB approximation for each mode using the same color but dashed lines. Deep inside this regime, computing exact mode functions is computationally expensive, so the adiabatic approximation is used instead, which smooths out oscillations and explains their absence in that region. The behavior of both  $\Pi_{\zeta 1}$  and  $\Pi_{\zeta 2}$  illustrate the approach to the super-SHS solution: Mode 1 reaches the constant  $\Pi_\zeta$  regime soon after exiting WKB, while Mode 2 shows a delayed approach due to its larger effective sound speed ( $c_\zeta \simeq 1/3$ ) relative to  $c_w = \sqrt{w} \ll 1$ . This contrast clarifies how the crossing of SHS regimes depends on the hierarchy between propagation speeds.

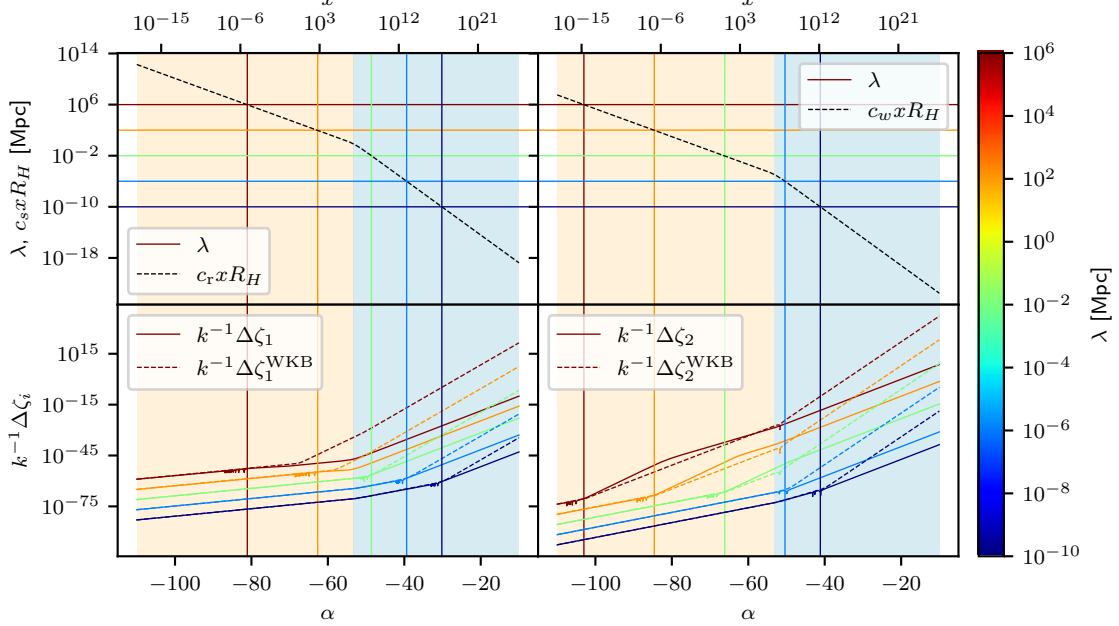


Figure 4. Evolution of the velocity isocurvature perturbation modes  $\Delta\zeta_i \propto Q_i$  (see Eq. (45)), analogous to Fig. 3 for the curvature perturbations  $\zeta_i$ . Top panels: comoving wavelength  $\lambda$  for each mode compared with the comoving Hubble radius multiplied by the relevant sound speed, with the extra factor  $k^{-1}$  separating the modes visually. Bottom panels: evolution of  $\Delta\zeta_1$  and  $\Delta\zeta_2$  across radiation- and matter-dominated eras. Vertical lines indicate sound-Hubble crossing ( $\lambda = c_i x R_H$ ), and only the real part of the mode functions is shown; deep inside this regime the adiabatic approximation smooths out oscillations.

power spectra scale as

$$k^3 |\bar{\Pi}_{\zeta 1}^{\times}|^2 \propto k^2, \quad (64)$$

$$k^3 |\bar{\Pi}_{\zeta 2}^{\times}|^2 \propto k^{\frac{12w}{1+3w}}. \quad (65)$$

Hence, only Mode 2 produces an almost scale-invariant spectrum, while Mode 1 has a steep blue spectrum with effective spectral index  $n = 3$ . Which mode dominates depends on the coefficients in Eq. (63). Mode 2 has a larger prefactor due to the presence of  $1/c_w^5$  and the presence of  $\Omega_r$  on Mode 1's prefactor. On the other hand, the spectrum of Mode 1 grows with  $k^2$  while Mode 2 grows with  $k^{\frac{12w}{1+3w}}$  which is a smaller exponent than 2 for  $w \ll 1$ . Thus, up to  $k = 1/R_{H_0}$ , Mode 2 dominates and then Mode 1 starts growing faster and would eventually overtake Mode 2. However, in practice, this overtaking occurs for modes that exit the WKB regime during or after the epoch of matter domination, and thus the approximations above will no longer hold. Nonetheless, for  $k \leq 1/R_{H_0}$ , Mode 2 provides a good approximation to the spectrum and we will use it to anchor the power spectrum at  $k = 1/R_{H_0}$ .

In our bounce scenario, contraction proceeds up to  $x_B = 10^{30}$  well inside the radiation-dominated era. Since  $\gamma_i$  is always a decreasing function of  $\alpha$ , the integrands of  $\mathcal{I}_i$  increase monotonically with time. In any single fluid dominated phases, they reduce to simple powers of  $x$ , so

the integrals can be split as

$$\int_{\alpha_i^{\times}(k)}^0 \frac{\gamma_i}{\gamma^2} d\alpha = \int_{\alpha_i^{\times}(k)}^{\alpha^*} \frac{\gamma_i}{\gamma^2} d\alpha + \int_{\alpha^*}^0 \frac{\gamma_i}{\gamma^2} d\alpha, \quad (66)$$

where  $\alpha_i^{\times}(k) = -s \ln [x_i^{\times}(k)/x_B]$ . The first term is bounded above by

$$\begin{aligned} \int_{\alpha_i^{\times}(k)}^{\alpha^*} \frac{\gamma_i}{\gamma^2} d\alpha &\leq [\alpha^* - \alpha_i^{\times}(k)] \frac{\gamma_i(\alpha^*)}{\gamma^2(\alpha^*)} \\ &\lesssim [\alpha^* - \alpha_i^{\times}(k)] \frac{3R_{H_0}}{4\sqrt{\Omega_r}} x^*. \end{aligned} \quad (67)$$

Here,  $\alpha^*$  is chosen such that the system is deep within the radiation-dominated phase. In this regime, the background functions simplify to

$$F_{\nu} \approx \frac{R_{H_0} k}{\sqrt{\Omega_r}} \frac{1}{x}, \quad (68)$$

$$\gamma_w \approx \frac{(1+w)\Omega_w}{R_{H_0}\sqrt{\Omega_r}} \frac{1}{x^{2-3w}}, \quad (69)$$

$$\gamma_r \approx \frac{4\sqrt{\Omega_r}}{3R_{H_0}} \frac{1}{x}. \quad (70)$$

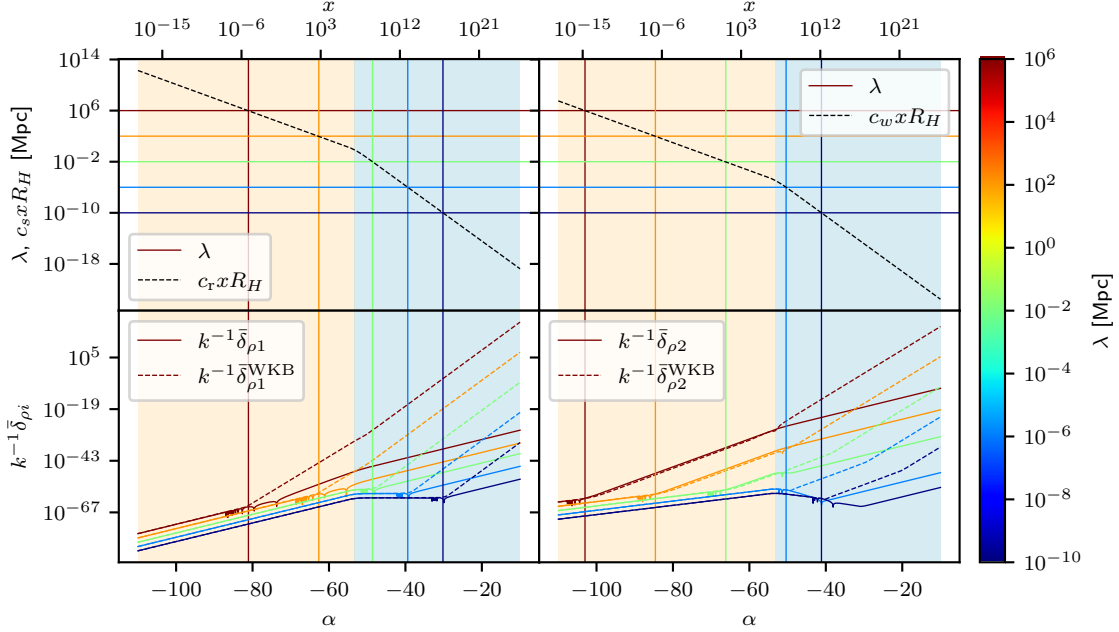


Figure 5. Evolution of the total energy density contrast  $\bar{\delta}_\rho$ , analogous to the previous figures. Top panels: comoving wavelength  $\lambda$  for each mode compared with the comoving Hubble radius multiplied by the relevant sound speed, with  $k^{-1}$  separating the modes visually. Bottom panels: evolution of  $\bar{\delta}_{\rho,1}$  and  $\bar{\delta}_{\rho,2}$  across radiation- and matter-dominated eras. Vertical lines indicate sound-Hubble crossing ( $\lambda = c_s x R_H$ ), and only the real part of the mode functions is shown; deep inside this regime the adiabatic approximation smooths out oscillations.

Accordingly, the late-time integrals are

$$\mathcal{I}_r \approx \int_{\alpha^*}^0 \frac{\gamma_r}{\gamma^2} d\alpha \approx \frac{3R_{H_0}}{4\sqrt{\Omega_r}}(x_B - x^*), \quad (71)$$

$$\mathcal{I}_w \approx \int_{\alpha^*}^0 \frac{\gamma_w}{\gamma^2} d\alpha \approx \frac{9R_{H_0}(1+w)\Omega_w}{16\Omega_r^{\frac{3}{2}}} \left( \frac{x_B^{3w} - x^{*3w}}{3w} \right). \quad (72)$$

Choosing, for instance,  $x^* = 10^{10} \ll x_B = 10^{30}$  (corresponding to the nucleosynthesis epoch) has two key effects: it ensures the first integral piece is negligible compared to the second, and it guarantees the background is in a pure radiation-dominated phase, allowing the second integral to be evaluated using the simple power-law approximations. Consequently, we find the late-time integrals are dominated by the endpoint at  $x_B$ , exhibiting negligible sensitivity to the transition time  $\alpha_i^\times(k)$ . This conclusion holds for all wavelengths that exit the sound-Hubble radius significantly before the end of contraction.

The integrands of all other integrals decrease monotonically in the radiation-dominated era, rendering them insensitive to the physics at the bounce scale. Consequently, the estimates derived in this section are all that is required to compute the super-SHS approximations (55). In practice, we estimate the large-scale power spectrum of  $\zeta$  using

$$\zeta(\alpha = 0) \approx c_r^2 \mathcal{I}_r \Pi_{\zeta 2}^\times, \quad (73)$$

leading to

$$\begin{aligned} \mathcal{P}_\zeta &= \frac{\ell_p^2 k^3}{2\pi^2} c_r^4 \mathcal{I}_r^2 |\Pi_{\zeta 2}^\times|^2, \\ &= \frac{\ell_p^2}{R_{H_0}^2} \frac{(1+w)x_B^2 \Omega_w^{2/(1+3w)}}{64\pi^2 \Omega_r c_w^{(5+3w)/(1+3w)}} (R_{H_0} k)^{\frac{12w}{1+3w}}, \\ &= 2 \times 10^{-32} \left( \frac{10^{-5}}{c_w} \right)^{\frac{5+3w}{1+3w}} (R_{H_0} k)^{\frac{12w}{1+3w}} \end{aligned} \quad (74)$$

where we reintroduced the  $\ell_p^2$  factor from (48). In the last equality, we used the fiducial cosmology parameters from (25), but we treat the factor  $c_w$  as a free parameter. Note that the amplitude is very small compared to the value expected from CMB observations. To achieve a power spectrum amplitude comparable to CMB observations, the value of  $c_w$  would need to be decreased to approximately  $10^{-10}$ . We do not use such values in our numerical integration because it becomes unstable for  $c_w \lesssim 10^{-5}$ . However, for such small values of  $c_w$ , all relevant quantities can be extrapolated from the numerics.

The exceedingly small amplitude of  $\mathcal{P}_\zeta$  stems from the prefactor  $(\ell_p/R_{H_0})^2 \propto 10^{-121}$ , which arises from imposing quantum initial conditions on cosmological scales. While the shear and expansion-rate perturbations possess a runaway growing mode during contraction, increasing as the scale factor decreases  $a \rightarrow a_B$  (equivalently  $x \rightarrow x_B$ ) and thereby enhancing the amplitude,

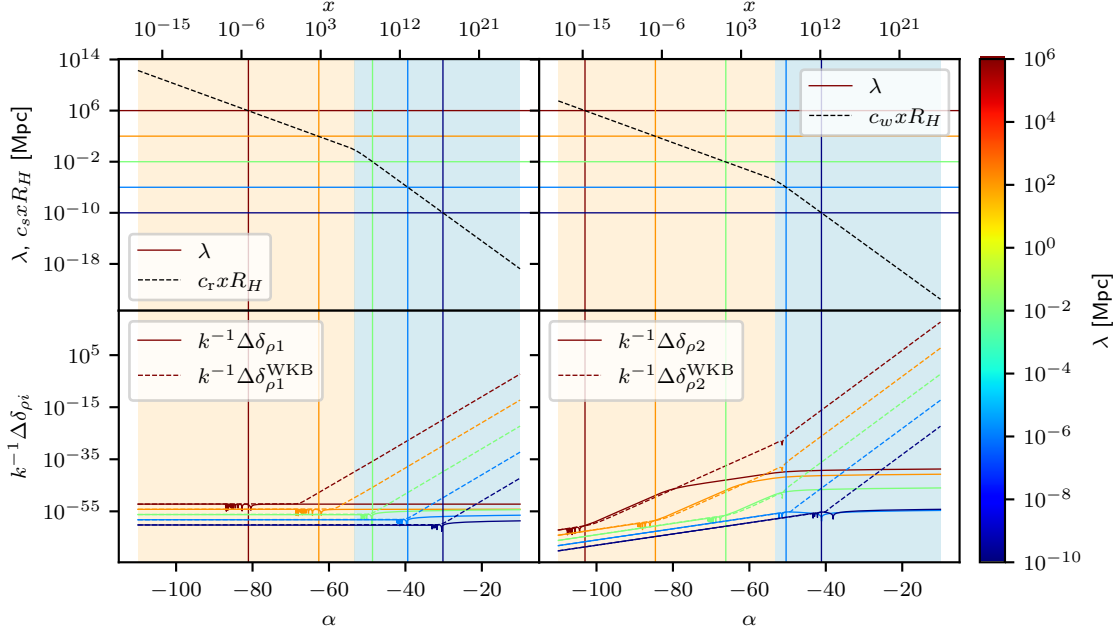


Figure 6. Evolution of the difference between the individual fluid energy density contrasts,  $\Pi_{Q_i} = \bar{\delta}_{\rho_{ri}} - \bar{\delta}_{\rho_{wi}}$ , analogous to Fig. 5 for the total energy density contrast. Top panels: comoving wavelength  $\lambda$  compared with the comoving Hubble radius times the relevant sound speed, with  $k^{-1}$  separating the modes visually. Bottom panels: evolution of  $\delta_{\rho_{ri}} - \delta_{\rho_{wi}}$  across radiation- and matter-dominated eras. Vertical lines indicate sound-Hubble crossing ( $\lambda = c_i x R_H$ ), and only the real part of the mode functions is shown; deep inside this regime the adiabatic approximation smooths out oscillations.

we are ultimately constrained by the requirement that the background curvature scale remain well above the Planck length  $\ell_p$ . This limits the maximum value of  $x_B$ . It is important to note that a comoving wavelength  $\lambda = R_{H_0}$  (a cosmological scale today) corresponds to a physical length of approximately  $10^{-4}$  m at the bounce, which is still significantly larger than  $\ell_p$ . Thus, the limitation on  $x_B$  is not imposed by the perturbations becoming trans-Planckian, but by the risk of the background curvature itself entering the full quantum gravity regime which would render inappropriate our use of the Wheeler DeWitt equation to describe the bounce.

It is important to stress that the super-SHS approximation can only be trusted when the relevant integral is dominated by one of its endpoints, i.e. for the initial time or at the bounce ( $\alpha = 0$ ). In general, we encounter two types of integrands, monotonically increasing or decreasing. In both cases the integrand evolves across many orders of magnitude within the time interval considered, but with different behaviors. For monotonically decreasing integrands, the dominant contribution comes from the initial time, where the super-SHS approximation is not very accurate. This is because at the starting point, the evolution matrix (A3) has Frobenius norm  $|M^n| > 1$  for all  $n$ , so the approximation is only slowly converging to the exact solution. The norm falls below unity only later in the evolution, which explains why the approximation performs better for monotonically increasing integrals. In this case, not only does the endpoint

at  $x_B$  provide the dominant contribution, but also, at the bounce time, one finds  $M(\alpha = 0)^n \ll 1$  for  $n > 1$ , ensuring that the initial-time contributions are strongly suppressed. Even so, accuracy is not guaranteed, since residual early-time evolution can significantly affect the constant part of the result. A concrete example is provided by curvature perturbations that cross the SHS close to or after equality, where the large value  $F_\nu = 1/c_w \gg 1$  for Mode 2 makes the sensitivity to the early-time dynamics manifest.

The super-SHS dynamics are especially relevant for Mode 2. This stems from the fact that the sound speed of the matter fluid is very small,  $c_w \ll 1$ . Consequently, the WKB regime for this mode ends when  $F_\nu = 1/c_w \gg 1$ . Moreover, Mode 2 is the dominant contributor to the large-scale power spectrum, so its evolution is of particular interest.

The super-SHS approximation follows from rewriting  $\dot{y} = My$  as the integral equation  $y(t) = y(t_0) + \int_{t_0}^t M(t') y(t') dt'$  and iterating it, so the expansion involves powers of the evolution matrix  $M$ . These powers contain terms of the form (cf. Eq. (48))

$$F_\nu^2 c_\zeta^2 \propto \frac{c_\zeta^2}{c_w^2}. \quad (75)$$

In this regime one has  $c_i F_\nu = \varepsilon \ll 1$ , and the approximation assumes that successive powers of  $M$  remain small. However, the super-SHS series includes the fac-

tor  $F_\nu^2 c_\zeta^2 = \varepsilon c_\zeta^2/c_i^2$ . For the first terms to be reliable one therefore needs

$$\varepsilon \frac{c_\zeta^2}{c_i^2} \lesssim 1.$$

Early in the super-SHS regime,  $\varepsilon$  is only slightly below unity. If the ratio  $c_\zeta^2/c_i^2$  is large at that time, the approximation using the first terms breaks down; it only becomes accurate later, when  $\varepsilon$  decreases.

This behavior is visible in Fig. 3. For Mode 1 the ratio  $c_\zeta^2/c_r^2$  remains controlled: it begins small ( $c_\zeta \simeq c_w$ ) and later approaches  $c_r$ , staying of order unity. As a result,  $\Pi_{\zeta 1}$  quickly approaches its constant super-SHS value after the WKB regime ends. For Mode 2,  $c_\zeta^2/c_w^2$  is of order unity only at the very beginning of the super-SHS regime but grows rapidly as  $c_\zeta$  approaches  $c_r$ . Consequently,  $\Pi_{\zeta 2}$  continues to evolve for some time after leaving the WKB regime and only later settles to a constant value. Notably, this early super-SHS evolution has a direct impact on the final value of  $\Pi_{\zeta 2}$  and is responsible for the corresponding reduction in the power-spectrum amplitude of  $\zeta_2$ .

Thus, when the total sound speed is still governed by the matter component ( $c_\zeta \approx c_w$ ) at WKB exit, the relevant contribution remains of order unity and the approximation yields a reasonable estimate for the power-spectrum amplitude. At later times, when radiation determines the sound speed ( $c_\zeta \approx c_r$ ), the same factor scales as  $c_r^2/c_w^2 \gg 1$ , leading to a situation where the first terms would not provide a good approximation and would require many terms to describe this time interval. Note however that numerically this regime is very well behaved and we compute it directly.

Therefore, we expect a reliable prediction only for modes that exit the WKB regime before the matter-radiation sound speed equality, defined by  $c_r^2 \gamma_r^2 = c_w^2 \gamma_w^2$ . This condition corresponds to the scale

$$x_s = \left[ \frac{c_w^2}{c_r^2} \frac{3(1+w)\Omega_w}{4\Omega_r} \right]^{1/(1-3w)}. \quad (76)$$

Using the definition of  $F_\nu$ , we obtain the associated wavenumber

$$k_2^s \equiv \frac{E(x_s)}{x_s c_w R_{H_0}} = \frac{\sqrt{3}\Omega_w}{2c_r \sqrt{\Omega_r} R_{H_0}} + \mathcal{O}(w). \quad (77)$$

It is important to note that  $x_s$  lies within the matter-dominated era. Thus, while the spectrum is affected by super-SHS evolution, the WKB regime still ends during matter domination. A second relevant scale for Mode 2 is  $\gamma_r = \gamma_w$ , given by

$$x_{\text{eq}} = \left[ \frac{3(1+w)\Omega_w}{4\Omega_r} \right]^{1/(1-3w)}. \quad (78)$$

The corresponding wavenumber, obtained again from Eq. (39), is

$$k_2^{\text{eq}} \equiv \frac{E(x_{\text{eq}})}{x_{\text{eq}} c_w R_{H_0}} = \frac{1}{c_w} \frac{\sqrt{21}\Omega_w}{4\sqrt{\Omega_r} R_{H_0}} + \mathcal{O}(w). \quad (79)$$

Beyond this scale, we no longer expect the nearly scale-invariant spectrum derived earlier to hold. The scales identified above, together with the predicted behavior of Mode 2 in the super-SHS regime, will be directly tested in the numerical analysis that follows.

## IV. RESULTS

We now present the results of the numerical integration of the coupled system of perturbation equations (48), using the initial conditions derived in Appendix A. Our analysis follows the evolution of perturbative modes through the contracting phase, across the bounce, and into the expanding phase. We pay particular attention to the resulting power spectra and their dependence on the model parameters.

### A. Evolution of Perturbative Modes

During the contracting phase, the background evolves from a dust-dominated regime to a radiation-dominated one. At the perturbative level, this implies that comoving wavelengths  $\lambda = 1/k$  exit the WKB regime at different stages: some during dust domination, others during radiation domination, and yet others during the transition between the two. In Appendix A, we established that the WKB scale is approximately given by  $c_i F_\nu$ .

Figure 3 illustrates this behavior for a range of modes. The top panels compare each mode's comoving wavelength with the corresponding SHS,  $c_i x R_H$ , making it easy to identify when modes leave the WKB regime and transition from sub- to super-Hubble evolution. The bottom panels show the time evolution of  $\zeta_1$  and  $\zeta_2$ , highlighting how the oscillatory behavior is suppressed once modes exit the SHS. Moreover, the WKB approximation plotted with dashed lines provides a reasonable description of modes in the WKB regime. Modes that exit during dust domination, radiation domination, or the transition exhibit the expected differences in phase and amplitude, consistent with the relative values of  $c_i F_\nu$  and the gravitational weights  $\gamma_i$  discussed in Sec. IV A.

Naturally, since we have two fluids, the curvature perturbation  $\zeta$  does not contain all the information about the system, and we also need to analyze the velocity entropy perturbation  $Q$ . As defined in Eq. (45), this variable is proportional to the difference between the curvature perturbations of each fluid:

$$Q_i \propto \Delta\zeta_i \equiv \zeta_{ri} - \zeta_{wi}. \quad (80)$$

Figure 4 shows the evolution of  $\Delta\zeta_i$ , analogous to Fig. 3 for the curvature perturbations  $\zeta_i$ . The qualitative behavior is similar: modes oscillate inside the SHS and evolve in a scale independent way once they exit. However, the amplitudes and phases differ, reflecting the distinct dynamics of isocurvature perturbations compared

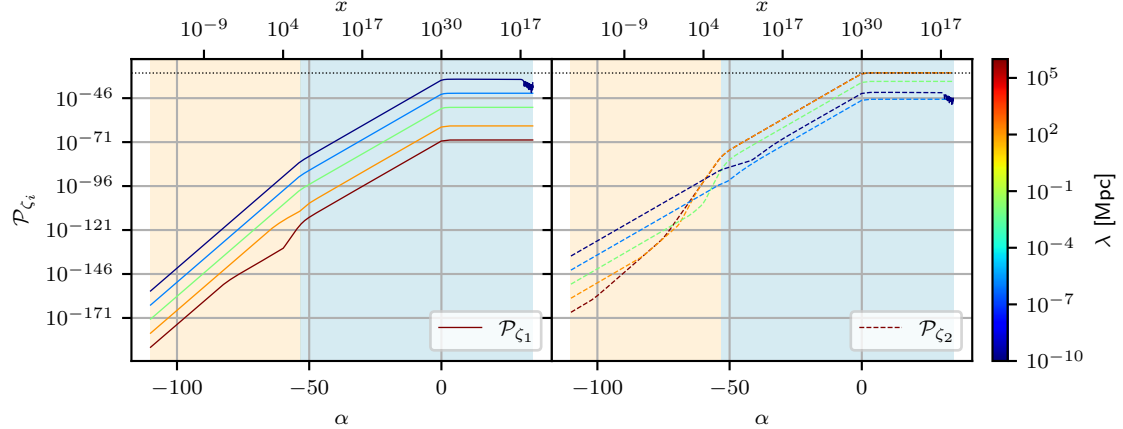


Figure 7. Time evolution of the curvature perturbation power spectrum  $\mathcal{P}_\zeta(k)$ , showing Mode 1 contributions (solid curves) and Mode 2 contributions (dashed curves). The color bar indicates comoving wavelength  $\lambda$  (in Mpc), with the top axis showing the corresponding scale factor  $x = a_0/a$ . Three key features emerge from the evolution: First, all modes begin with a characteristic  $k^2$  (blue-tilted) power spectrum, apparent from the larger amplitudes at smaller wavelengths. Second, Mode 2 displays irregular evolution - longer wavelengths that exit the SHS during matter domination (brown/red curves) undergo significant amplitude enhancement compared to modes that exited during radiation domination. Third, Mode 1 maintains its blue-tilted spectral shape throughout the entire evolution, showing no comparable amplification. These distinct behaviors reflect fundamentally different dynamics dependent on the SHS crossing time. The dotted line shows the approximate analytic result from Eq. (74) evaluated at  $k = 1/R_{H_0}$ .

to curvature ones. Comparing Figs. 3 and 4, one sees that both  $\zeta_i$  and  $\Delta\zeta_i$  grow during the contracting phase, leading to a corresponding perturbation in the fluid velocities. This illustrates how the coupled two-fluid system naturally generates both curvature and isocurvature perturbations during contraction.

Now, the momenta  $\Pi_{\zeta_i}$  and  $\Pi_{Q_i}$  are also relevant, as they characterize the dynamics of the perturbation energy densities. They are given by Eqs. (43) and (46), respectively. Using these expressions, we compute the total energy density contrast  $\bar{\delta}_\rho$ , Eq. (42), and the difference between the individual fluid contrast,  $\bar{\delta}_{\rho r} - \bar{\delta}_{\rho w}$ , which is given directly by the momenta  $\Pi_{Q_i}$ . Figure 5 shows the evolution of  $\bar{\delta}_\rho$ , which exhibits oscillations inside the SHS and freezes outside, similarly to  $\zeta_i$  and  $\Delta\zeta_i$ . The amplitude of the total energy density grows during contraction, indicating that the energy density perturbations become significant.

By contrast, the isocurvature perturbations, defined as the difference between the fluid energy density contrasts, are dynamically suppressed relative to the curvature ones, as shown in Fig. 6. While they also oscillate inside the SHS and evolve in a scale independent way, their amplitude remains much smaller than that of the total energy density contrast. Thus, although entropy perturbations are generated during contraction, they do not grow significantly. This behavior is consistent with the expectation that the curvature perturbations dominate, while isocurvature modes remain subdominant. A direct comparison between Figs. 5 and 6 shows that the isocurvature modes are suppressed by several orders of

magnitude relative to the curvature ones.

Having analyzed all perturbative modes, we can now summarize their dynamics. Mode 1 evolves according to the SHS  $c_r x R_{H_0}$ , while Mode 2 follows  $c_w x R_{H_0}$ . In the WKB regime, their amplitudes generally grow (with the exception of  $\Delta\bar{\delta}_{\rho 1}$ ), as seen from the leading terms in Eqs. (A9) and (A10).

The canonical momentum  $\Pi_{Q1}$ , however, behaves differently. Its leading WKB amplitude is

$$|\bar{\Pi}_{Q1}| = \sqrt{\frac{F\nu}{2c_r \gamma_r}} = \sqrt{\frac{3k}{8c_r \Omega_r}}, \quad (81)$$

where we have used Eqs. (39) and (36) to substitute the gravitational weight  $\gamma_r$ . Unlike other perturbations,  $\bar{\Pi}_{Q1}$  remains constant throughout the WKB regime, implying a time-independent contribution to the entropy perturbation during this phase.

Thus, while all other perturbation modes grow during sub-Hubble evolution in the contracting phase,  $\Pi_{Q1}$  stays approximately constant. After SHS exit, all modes enter the super-Hubble regime. An exception is  $\Pi_{Q2}$ , which exhibits a transient evolution before reaching its asymptotic constant value. This illustrates the super-SHS dynamics discussed earlier, where early-time effects and the action of the evolution matrix  $M$  can shift the constant part of the solution, particularly for modes sensitive to initial conditions.

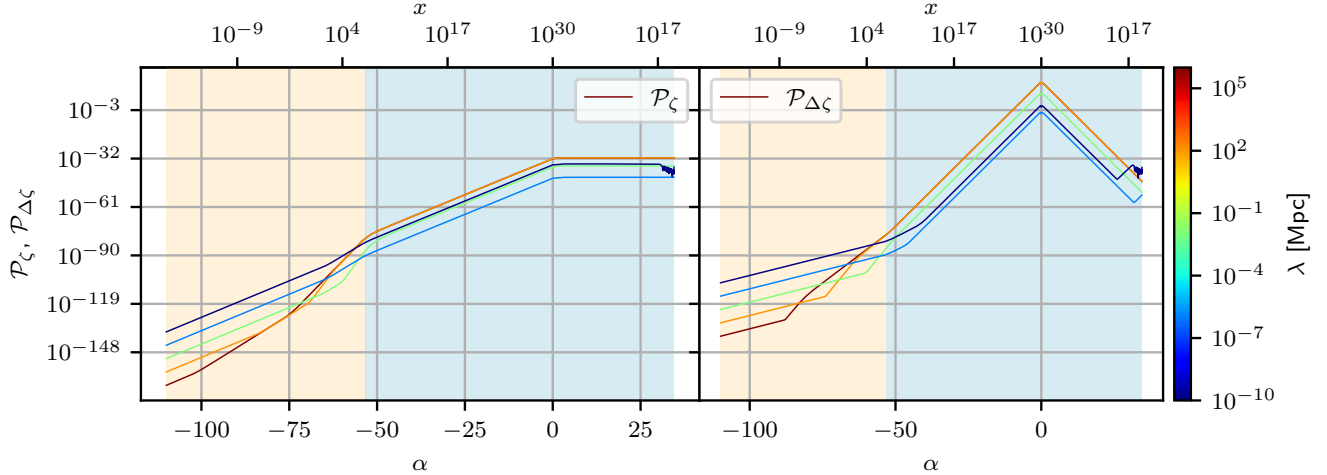


Figure 8. Time evolution of the total curvature perturbation power spectrum  $\mathcal{P}_\zeta(k)$  (left panel) and the associated isocurvature spectrum  $\mathcal{P}_{\Delta\zeta}(k)$  (right panel), combining contributions from both Mode 1 and Mode 2. The color bar indicates the comoving wavelength  $\lambda$  (in Mpc), and the top axis shows the corresponding scale factor  $x = a_0/a$ . The curvature spectrum  $\mathcal{P}_\zeta(k)$  evolves from an initially blue-tilted  $k^2$  shape to a final form characterized by a nearly scale-invariant plateau at large scales (long wavelengths) and a pronounced decline at small scales (short wavelengths). This evolution reflects the different amplification of modes depending on their SHS crossing epoch: modes exiting during matter domination are amplified to form the plateau, while those exiting during radiation domination retain their blue tilt with reduced amplitude. The resulting spectrum encodes the interplay between the two fluid components during the contracting phase. The isocurvature spectrum  $\mathcal{P}_{\Delta\zeta}(k)$  also begins with a blue tilt but evolves into a mixed spectrum at late times. Although it can temporarily exceed the curvature spectrum around the bounce, its amplitude decreases afterward, eventually becoming smaller than  $\mathcal{P}_\zeta(k)$ .

## B. Power Spectra Evolution

Our analysis of individual perturbation modes now leads us to their observable consequences, namely the primordial power spectra that govern cosmic structure formation. These spectra encode the statistical properties of three fundamental quantities: the curvature perturbation  $\zeta$  that seeds large-scale structure formation, the velocity isocurvature perturbation  $\Delta\zeta = \zeta_r - \zeta_w$  that captures fluctuations between radiation and matter components, and the energy density contrasts  $\bar{\delta}_\rho$  and  $\bar{\delta}_{\rho r} - \bar{\delta}_{\rho w}$  that describe energy density isocurvature perturbations.

In Fig. 7, we show the time evolution of the curvature perturbation power spectrum  $\mathcal{P}_\zeta(k)$ , distinguishing between Mode 1 (solid curves) and Mode 2 (dashed curves). Three key features characterize the dynamics: First, all modes initially follow a  $k^2$  (blue-tilted) power spectrum, evidenced by the enhanced amplitudes at smaller wavelengths. Second, Mode 2 exhibits scale-dependent evolution: longer wavelengths crossing the SHS during matter domination (brown/red curves) undergo significant amplification compared to those crossing during radiation domination (blue/green curves). After SHS crossing, these modes asymptote to a nearly scale-invariant spectrum.

In contrast, Mode 1 preserves its blue-tilted spectral shape throughout the evolution. Since shorter wavelengths of Mode 2 remain unamplified, the total spectrum becomes Mode 1-dominated at small scales. This

contrast between modes, with their amplification sensitive to the SHS crossing epoch, demonstrates the necessity of including both contributions to fully capture the curvature perturbation's dynamics.

In order to help interpret these results, in Fig. 8 we show the evolution of the total curvature perturbation power spectrum  $\mathcal{P}_\zeta(k)$ . Note that large wavelengths leave the SHS during dust domination and are amplified and join in an almost scale invariant spectrum, while small wavelengths leave during radiation domination and remain blue tilted. However, since the latter have a smaller amplitude, the final effect is a large decrease in power for small scales followed by a blue spectrum.

The right panel of Fig. 8 shows the evolution of the isocurvature perturbation power spectrum  $\mathcal{P}_{\Delta\zeta}(k)$ . Similar to the curvature spectrum, it is initially blue-tilted and evolves into a mixed spectrum at late times. The overall amplitude remains suppressed relative to the curvature power spectrum, as expected. One might question whether the temporary enhancement of the isocurvature amplitude around the bounce could indicate a breakdown of the linear approximation. However, as discussed in [34], linear theory remains valid as long as perturbations are small in the chosen gauge. In Sec. IV D, we show that in the constant-curvature gauge the isocurvature perturbation remains linear through the bounce and becomes further suppressed afterward.

### C. Curvature Power Spectrum

We present the adiabatic curvature power spectrum  $\mathcal{P}_\zeta(k)$  for the two-fluid model, computed numerically and shown in Fig. 9. At long wavelengths, the analytic approximation in Eq. (74) provides a reasonable estimate of both amplitude and spectral index,

$$n_s(w) = 1 + \frac{12w}{1 + 3w}, \quad (82)$$

predicting an almost scale-invariant spectrum in this regime.

For shorter wavelengths, the SHS crossing occurs closer to the matter-radiation transition, leading to a suppression of the amplitude before the spectral index reaches  $n_s = 3$  (see Eq. (64)) and producing an overall red tilt in the mean spectrum. This suppression begins at the scale  $k_2^s$ , Eq. (77), when the sound speed in the matter-dominated era starts to increase (from  $\sqrt{w}$  to  $1/\sqrt{3}$ ), and ends at the scale  $k_2^{eq}$ , Eq. (79), corresponding to the background transition from matter to radiation domination. These two scales are indicated as vertical lines in Fig. 9, where one can see that both scales correctly mark the transition for the power spectrum shape.

Since the curvature spectrum becomes constant shortly after the bounce, the precise time at which it is evaluated is irrelevant. In contrast, as we will see in the next section, the isocurvature power spectrum generally depends on time, requiring a specific evaluation epoch. Here we adopt  $x = 1 + z = 10^{15}$ , corresponding to a time well after the bounce and well above the nucleosynthesis redshift ( $z \simeq 10^{10}$ ).

In Fig. 10, we focus on scales relevant for the CMB and quantify the spectral shape using both linear and quadratic fits in  $\ln k$ . We adopt the pivot scale  $k_0 = 0.05 \text{ Mpc}^{-1}$ , consistent with Planck 2018 [35], and parametrize the spectrum as

$$n_s(k) = n_{\text{eff}} + \frac{1}{2} \alpha_s \ln \frac{k}{k_0}, \quad (83)$$

where  $\alpha_s \equiv dn_s/d \ln k$  is the running of the spectral index. The fits yield

- Linear (constant  $n_s$ ):  $n_{\text{eff}} = 0.9851$ .
- Quadratic (allowing for running):  $n_{\text{eff}} = 0.9514$ ,  $\alpha_s = -0.0086$ .

The running captures the mild scale dependence across the CMB scales ( $k \lesssim 1 \text{ Mpc}^{-1}$ ), mainly due to the loss of amplitude at short scales. While these numbers are close to those obtained by Planck, they arise from fitting a spectrum that is not inherently polynomial; thus, a quadratic approximation is only indicative. A proper comparison with observations requires a full statistical analysis using the numerical spectrum directly.

At first glance, the fact that the spectrum is not a simple power law with  $n_s \approx 0.96$  might seem like a shortcoming of the model. However, as emphasized by the Planck

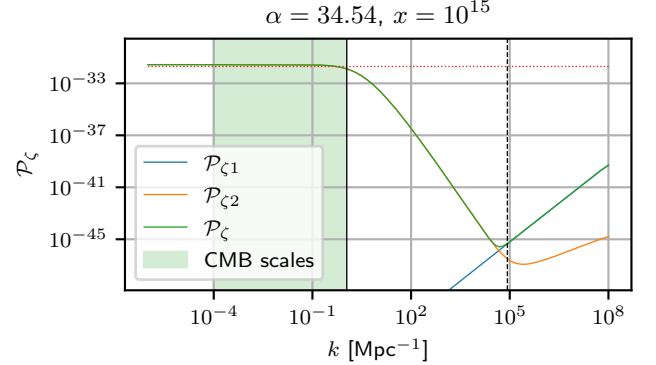


Figure 9. Power spectrum  $\mathcal{P}_\zeta(k)$  of adiabatic perturbations in the two-fluid model. The spectrum exhibits two approximate power-law regimes associated with matter and radiation domination, separated by a transition interval  $k_2^s < k < k_2^{eq}$ . These scales are shown as vertical lines in the plot:  $k_2^s$  (solid) and  $k_2^{eq}$  (dashed). The CMB-relevant scales ( $10^{-4} \text{ Mpc}^{-1} < k < 1 \text{ Mpc}^{-1}$ ) are highlighted in green.

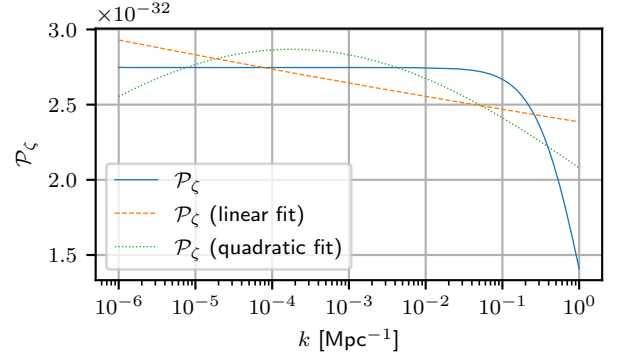


Figure 10. Figure showing the curvature power spectrum for  $\mathcal{P}_\zeta(k)$ , localized for the CMB  $10^{-6} < k < 1$ . We included a linear and quadratic fits, resulting in  $n_s = 0.9851$  and  $n_s = 0.9514$  with running parameter  $\alpha_s = -0.0086$ .

collaboration [36], a model-independent reconstruction of the primordial power spectrum from CMB data does not require a red-tilted power law.<sup>4</sup> Indeed, examining Fig. 20 of [36], one sees that a spectrum that is approximately scale-invariant at large scales with a mild suppression of power at smaller scales appears to be compatible with the data. A definitive assessment, however, requires a full statistical analysis and, ideally, a model comparison using the numerical spectrum.

<sup>4</sup> A power law with  $n_s \approx 0.96$  is *consistent* with current observations, but not uniquely preferred.

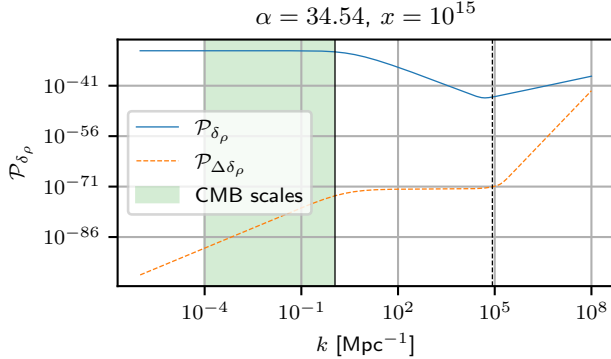


Figure 11. Power spectrum of isocurvature perturbations in the two-fluid model, computed at  $x = 10^{15}$  during the expanding phase. The spectrum, obtained from Eqs. (42) and (46), shows that the isocurvature amplitude is strongly suppressed relative to the curvature spectrum, although it approaches it at very small scales due to its steeper slope.

#### D. Isocurvature Perturbations

To compute the CMB temperature power spectrum, we must also consider possible isocurvature perturbations. In standard single-field inflation, such perturbations are not generated during the inflationary phase, since the dynamics is governed by a single degree of freedom, but can be produced after inflation, e.g. during the reheating phase, when different components may acquire distinct density fluctuations. In contrast, multi-field inflationary models naturally allow isocurvature modes to be generated already during inflation. Current observations from Planck [35] show that isocurvature contributions to the CMB power spectrum are very small: they have only been constrained, not measured.

In the two-fluid model, the isocurvature perturbations are obtained from the total energy density (42) and its associated perturbation (46). The resulting power spectrum is shown in Fig. 11. The plot indicates that, for the quantities defined by Eqs. (42) and (46), the isocurvature amplitude is strongly suppressed compared to the curvature one. Nonetheless, the isocurvature spectrum is steeper and approaches the curvature spectrum at very small scales. This behavior implies that the near absence of large-scale isocurvature perturbations is a natural prediction of the model, consistent with observations, without invoking additional mechanisms such as those required during reheating.

Note, however, that this isocurvature power spectrum is computed at the same time as the adiabatic one ( $x = 10^{15}$ ). To assess its time dependence, we also evaluate both spectra at the bounce ( $\alpha = 0.01$ ,  $x \approx a_B$ ). The corresponding power spectrum is shown in Fig. 12. As seen for  $\bar{\delta}_\rho$  and  $\Delta\bar{\delta}_\rho$ , the isocurvature power spectrum remains smaller than the curvature one at all times. The behavior of the isocurvature power spectrum differs significantly from that of the curvature perturbations.

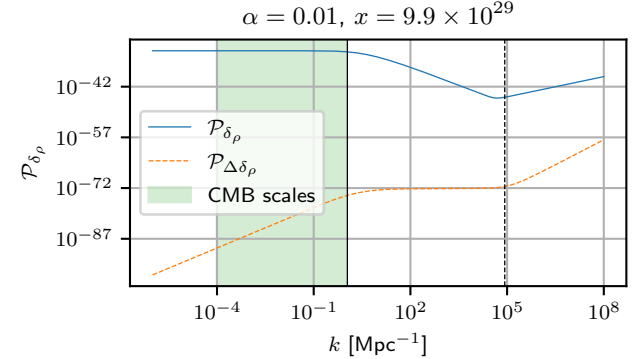


Figure 12. Power spectrum of isocurvature perturbations in the two-fluid model, computed near the bounce ( $\alpha = 0.01$ ,  $x \approx a_B$ ) during the expanding phase. As in Fig. 11, the isocurvature amplitude, derived from Eqs. (42) and (46), remains strongly suppressed relative to the curvature spectrum, despite becoming comparable at very small scales due to its steeper slope. Even at the bounce, the isocurvature power spectrum remains well below the curvature one. As seen in Fig. 11, the main difference is that the isocurvature spectrum increases at smaller scales after the bounce, leading to a noticeably steeper dependence on  $k$ .

While the energy density contrast  $\bar{\delta}_\rho$  remains suppressed at all times, the adiabatic perturbations  $\zeta$  are enhanced around the bounce, as shown in Fig. 8. In particular, the isocurvature power spectrum can reach amplitudes  $\Delta\zeta > 1$ .

This can be understood by noting that  $\zeta$  is a weighted combination of the individual fluid perturbations  $\zeta_w$  and  $\zeta_r$ , Eq. (40). Even if  $\zeta_w$  grows very large, the total  $\zeta$  can remain small during the radiation dominated phase because  $\gamma_w \ll \gamma$ , so that the combination  $\gamma_w\zeta_w/\gamma$  is suppressed. As a result,  $\zeta_w$  grows rapidly during contraction and decreases rapidly during expansion, while the total  $\zeta$  remains moderate.

Evaluating these quantities in a specific gauge further clarifies the behavior around the bounce and confirms that the linear regime is maintained. Using the physical velocity perturbation defined in Eq. (44), Fig. 13 shows that the isocurvature velocity perturbation is enhanced during contraction but becomes suppressed during expansion, eventually vanishing while never exceeding unity. The left panel illustrates that the matter isocurvature velocity perturbation grows during contraction but remains below one, while the right panel shows that both velocity potentials converge to the same spectrum during expansion, indicating the strong suppression of isocurvature velocity perturbations in this phase. This behavior is also evident at the very end of the evolution of  $\Delta\zeta$  in Fig. 8, where it decreases below the curvature spectrum at late times.

Finally, although the perturbations undergo a complex evolution during contraction, the bounce, and the subsequent expansion, the resulting spectrum shown in Fig. 10

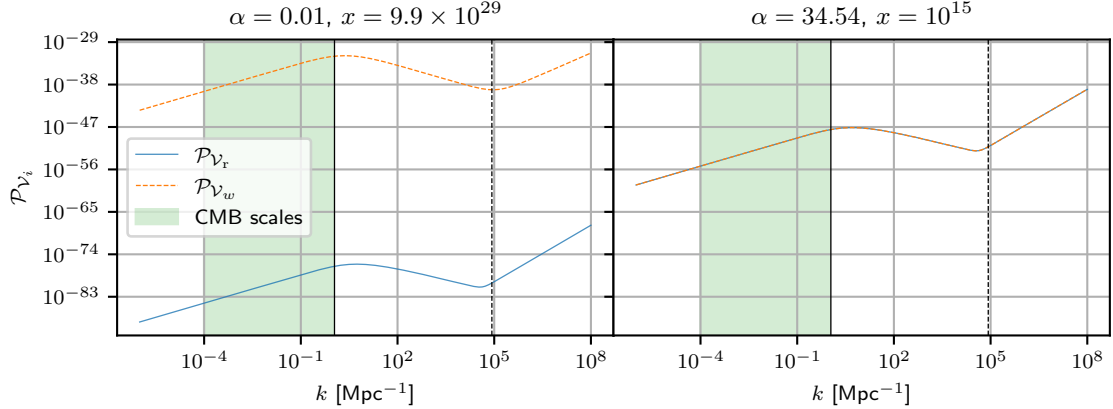


Figure 13. Power spectrum of the fluid velocity perturbations  $kx\mathcal{V}_w$  and  $kx\mathcal{V}_r$  in the two-fluid model (see Eq. (44)), computed near the bounce ( $\alpha = 0.01$ ,  $x \approx a_B$ , left panel) and during the expanding phase ( $x = 10^{15}$ , right panel). Near the bounce,  $kx\mathcal{V}_w$  is enhanced during contraction, while  $kx\mathcal{V}_r$  grows more slowly, producing a significant difference in the power spectra. During the expanding phase, both velocity perturbations converge to the same spectrum, reflecting the suppression of isocurvature velocity perturbations.

is compatible with negligible isocurvature perturbations at the onset of CMB evolution, at least for the scales relevant to the CMB power spectrum, as we will see in the following sections. Consequently, the computation of the CMB angular power spectrum can be done in the same way as what is done for an inflationary scenario, namely using only the primordial power spectrum, here provided from Fig. 10. Although the correlation between curvature and isocurvature perturbations can be strong in terms of the correlation coefficient, the actual covariance is negligible due to the suppressed isocurvature amplitude. As a result, cross-correlation terms do not significantly contribute to the CMB power spectrum and can be safely ignored.

### E. Tensor Perturbations

Having established the behavior of scalar perturbations, including the red tilt and power suppression at small scales, we now examine whether primordial gravitational waves remain consistent with observational constraints. This requires analyzing tensor perturbations and the tensor-to-scalar ratio  $r$ .

Tensor perturbations in two-fluid bouncing cosmologies were previously studied in [37] for radiation plus a perfect dust fluid with  $w = 0$ . Since we consider an almost pressureless fluid with  $w \ll 1$ , we expect qualitatively similar behavior, though the details differ due to our specific background evolution.

Tensor perturbations  $h_{\lambda k}$  evolve according to the equations of motion [37, 38] (see also Ref. [39])

$$h''_{\lambda k} + 2\frac{m'_h}{m_h}h'_{\lambda k} + \nu_{\text{rk}}^2 h_{\lambda k} = 0, \quad (84)$$

where  $\lambda = +, \times$  refers to the polarization of the tensor

perturbation and we introduced the effective masses and frequencies

$$m_h^2 \equiv \frac{a^3}{N}, \quad (85a)$$

$$\nu_{\text{rk}}^2 \equiv \left(\frac{Nk}{a}\right)^2, \quad (85b)$$

where  $N$  is the lapse function [38].

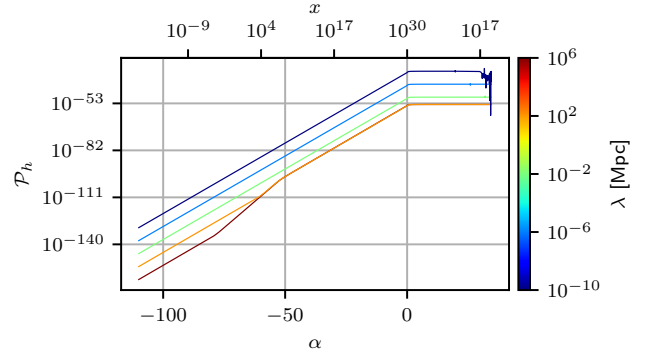


Figure 14. Time evolution of the tensor power spectrum  $\mathcal{P}_h(k)$  for different comoving wavelengths  $\lambda$  (in Mpc), with the corresponding scale factor  $x = a_0/a$  shown on the top axis. Modes crossing the Hubble radius during matter domination (brown/red) exhibit different evolution from those exiting during radiation domination (blue/green), though both freeze out after horizon crossing.

Unlike scalar perturbations, where the two fluids contribute coupled modes, tensor perturbations are decoupled and evolve independently for each polarization  $\lambda = +, \times$ . This decoupling allows us to quantize the system using a standard adiabatic vacuum prescription, setting

initial conditions deep in the contracting phase where modes are well inside the Hubble radius. We then evolve the modes numerically through the bounce and into the expanding phase, following the procedure detailed in Ref. [37].

The dimensionless tensor power spectrum is defined as

$$\mathcal{P}_h(k) = \frac{1}{2\pi^2} k^3 \sum_{\lambda=+,\times} |h_{\lambda k}|^2, \quad (86)$$

where the sum accounts for both polarization states. Figure 14 shows the evolution of  $\mathcal{P}_h(k)$  for representative modes. As in the scalar case, the spectrum exhibits two distinct behaviors depending on whether modes cross the Hubble radius during matter or radiation domination. However, here we have a crucial difference, tensor perturbations propagate at the speed of light, whereas scalar perturbations have a varying sound speed. Consequently, the transition between the two regimes is governed solely by Hubble crossing rather than SHS crossing, leading to qualitatively different dynamics.

The final tensor power spectrum, computed at  $x = 10^{15}$  during the expanding phase and shown in Fig. 15, exhibits a nearly scale-invariant spectral index at CMB scales, transitioning to a steeper slope ( $n_T \approx 3$ ) at smaller scales. Notably, unlike the scalar spectrum, there is no power suppression for modes crossing during radiation domination, and the spectrum simply changes slope at the transition scale.

To assess observational viability, we compute the tensor-to-scalar ratio, defined as

$$r(k) \equiv \frac{\mathcal{P}_h(k)}{\mathcal{P}_\zeta(k)}, \quad (87)$$

and plotted in Fig. 16. At CMB scales, the tensor amplitude is substantially smaller than the scalar one, yielding  $r \sim 10^{-22}$ , which lies about 22 orders of magnitude beneath the Planck bound  $r \lesssim 0.10$  [36]. This demonstrates that primordial gravitational waves do not threaten the viability of the two-fluid model. Consequently, tensor perturbations can be safely neglected when computing CMB temperature and polarization predictions.

While tensor perturbations are negligible at CMB scales, the situation changes at smaller scales. As Figs. 14 and 16 show, the tensor-to-scalar ratio increases significantly in this regime, reaching  $r(k) \sim 10^3$  for the smallest scales. This behavior arises from two factors: the continuous growth of the tensor spectrum and the suppression of scalar power at small scales discussed in Sec. IV D. Beyond the transition scale, both spectra have similar slopes, so  $r(k)$  plateaus at this elevated value.

This enhancement suggests that the model's primordial gravitational waves could be detectable by gravitational wave observatories sensitive to smaller wavelengths, such as LISA or pulsar timing arrays like NanoGrav. We defer a detailed analysis of these predictions to future work.

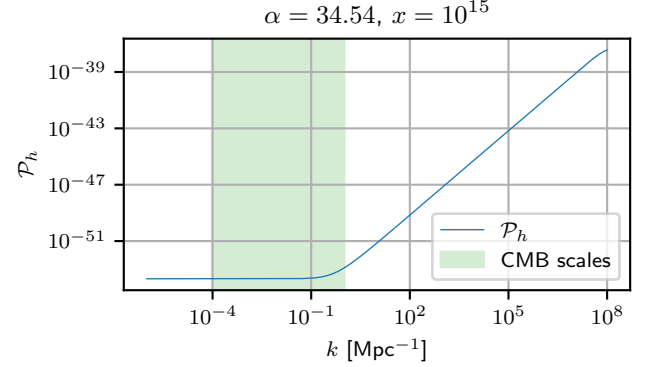


Figure 15. Tensor power spectrum  $\mathcal{P}_h(k)$  computed at  $x = 10^{15}$  during the expanding phase. The spectrum is nearly scale-invariant at large scales (CMB regime) and transitions to a steeper slope ( $n_T \approx 3$ ) at smaller scales, with no suppression at the transition unlike the scalar spectrum.

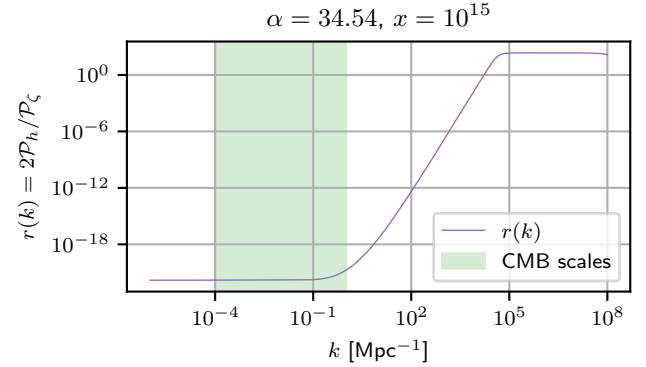


Figure 16. Tensor-to-scalar ratio  $r(k)$  as a function of co-moving wavelength  $\lambda$  (in Mpc). At CMB scales,  $r \sim 10^{-22}$ , safely below Planck constraints [36]. The ratio increases dramatically at smaller scales, reaching  $r(k) \sim 10^3$ , where gravitational waves may be detectable by LISA or pulsar timing arrays.

## F. Angular Power Spectra

Having computed the primordial power spectra, we now outline how these results can be connected to observations. Given the theoretical scope and length of the present work, we do not attempt a full statistical analysis here. Instead, the goal of this section is to demonstrate how the primordial curvature power spectrum produced by the model can be efficiently parametrized and incorporated into standard cosmological pipelines.

Using this parametrization, we illustrate how the model can be interfaced with Boltzmann codes and observational pipelines. As an example, we show the resulting angular power spectra and report a representative best-fit to Planck 2018 data. A complete statistical analysis, including full MCMC sampling and updated constraints, will be presented in a forthcoming companion paper.

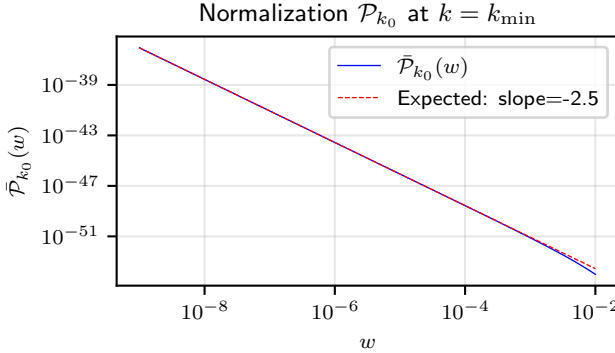


Figure 17. Scaling of  $\bar{\mathcal{P}}_\zeta(\kappa = 10^{-3}; w)$  with  $w$ , verifying the expected  $w^{-5/2}$  dependence. Deviations for  $w \gtrsim 10^{-3}$  arise from higher-order corrections in  $w$ .

Our parametrization strategy exploits the analytical insights from Sec. IV C. Recall that at large scales, the approximate expression in Eq. (74) gives the amplitude at leading order in  $w$  as

$$\mathcal{P}_\zeta(k) \propto \frac{\ell_p^2 x_B^2 \Omega_w^2}{R_{H_0}^2 \Omega_r c_w^5} \equiv q_A, \quad (88)$$

while the transition scale  $k_2^s$  marking the onset of the red tilt (see Eq. (77)) scales as

$$R_{H_0} k_2^s \propto \frac{\Omega_w}{\sqrt{\Omega_r}} \equiv q_k. \quad (89)$$

These two quantities, illustrated in Fig. 9, control the leading-order dependence on model parameters:  $q_A$  sets the overall amplitude, while  $q_k$  determines the characteristic scale of spectral features. However, the full spectrum also depends non-trivially on  $w$  through the large-scale tilt and the detailed shape of the transition region.

To capture this additional  $w$ -dependence efficiently, we precompute the full numerical power spectrum on a dimensionless grid. Introducing the variable

$$\kappa \equiv R_{H_0}^F k, \quad (90)$$

we evaluate the numerical spectrum  $\bar{\mathcal{P}}_\zeta(\kappa; w)$  for

$$10^{-9} \leq w \leq 10^{-1}, \quad 10^{-3} \leq \kappa \leq 10^8,$$

using logarithmically spaced sampling in both variables. All remaining parameters are fixed at fiducial values  $\Omega_r^F = 10^{-5}$ ,  $x_B^F = 10^{30}$ , and  $H_0^F = 70 \text{ km s}^{-1} \text{ Mpc}^{-1}$ .

This scan serves two purposes. First, it allows us to verify the expected analytical scaling. In particular, the spectrum evaluated at the fixed super-Hubble scale  $\kappa = 10^{-3}$  follows the predicted power law

$$\bar{\mathcal{P}}_\zeta(10^{-3}; w) \propto w^{-5/2}, \quad (91)$$

as shown in Fig. 17. This confirms the leading-order behavior of the amplitude factor  $q_A$ .

Second, this computation isolates the residual shape dependence of the spectrum. We define the dimensionless shape function

$$f(\kappa, w) \equiv \frac{\bar{\mathcal{P}}_\zeta(\kappa; w)}{\bar{\mathcal{P}}_\zeta(10^{-3}; w)}, \quad (92)$$

which satisfies  $f(10^{-3}, w) = 1$  by construction and depends only on the spectral shape. In practice,  $f(\kappa, w)$  is represented by a two-dimensional spline interpolant in  $(\log \kappa, \log w)$ .

The primordial power spectrum can then be written as

$$\mathcal{P}_\zeta(k; w, A_s, k_0) = A_s f\left(\frac{k}{k_0}, w\right), \quad (93)$$

where the effective amplitude and scale parameters are

$$A_s = \bar{\mathcal{P}}_\zeta(10^{-3}; w) \frac{q_A}{q_A^F}, \quad (94)$$

$$k_0 = \frac{q_k}{R_{H_0} q_k^F}. \quad (95)$$

This parametrization captures the dependence of the spectrum on  $\Omega_r$ ,  $x_B$  and  $H_0$  through  $(A_s, k_0)$ , while the parameter  $w$  controls the remaining shape dependence encoded in  $f$ . We have verified that it reproduces the full numerical spectrum to excellent accuracy throughout the parameter ranges of interest, provided  $w \ll 1$  and the transition scale  $k_2^s$  remains within the computed domain.

Another relevant feature of this model is that, within the CMB window, the primordial power spectrum probes only the onset of the transition between its two asymptotic regimes. As shown in Figs. 9 and 10, CMB scales span only the initial part of the transition from the nearly scale-invariant large-scale regime to the strongly blue-tilted small-scale regime. As a consequence, current CMB data are not expected to place strong constraints on values of  $w \ll 1$ . Instead, they primarily provide an upper bound on  $w$  consistent with the observed spectra.

In this regime, the dominant sensitivity to  $w$  enters through the amplitude parameter  $q_A$ . However, this dependence is degenerate with that of other model parameters. By contrast, the scale parameter  $k_0$  is mainly sensitive to  $\Omega_r$ , since  $H_0$  is already tightly constrained by CMB data alone. Therefore, while  $k_0$  effectively constrains  $\Omega_r$ , the amplitude parameter  $A_s$  constrains a combination of  $w$  and  $x_B$ . This leads to a degeneracy in the  $(w, x_B)$  plane.

For this reason, when translating the representative best-fit results into constraints on the underlying physical parameters, we compute the translation as function of  $x_B$ . The radiation density parameter  $\Omega_r$  can then be inferred from the fitted scale parameter  $k_0$  by inverting Eq. (95), yielding

$$\Omega_r = \left( \frac{\sqrt{1 + 4B^2} - 1}{2B} \right)^2, \quad B \equiv \frac{1}{q_k^F k_0 R_{H_0}}. \quad (96)$$

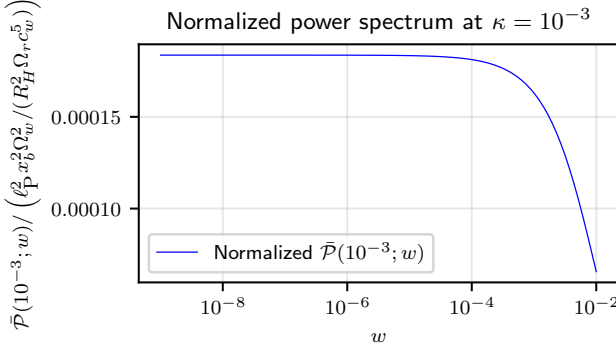


Figure 18. The normalized primordial power spectrum evaluated at  $\kappa = 10^{-3}$ . Note that all parameters are fixed at their fiducial values except for  $w$ . For  $w \lesssim 10^{-3}$ , the spectrum follows the expected  $w^{-5/2}$  scaling and this normalization factor  $\mathcal{A}_0$  remains approximately constant, simplifying the inversion for  $w$  from  $A_s$ .

In order to invert for  $w$ , we need to use Eq. (94) to express  $w$  in terms of  $A_s$ . However, there is a complicated dependence on  $w$  through the shape function  $f$ . Nonetheless, since  $w$  is expected to be small in the CMB window, the Fig. 17 shows that for  $w \lesssim 10^{-3}$ , the factor  $\mathcal{A}_0 \equiv \bar{\mathcal{P}}_\zeta(10^{-3}; w)/q_A^F$  is approximately constant. For our fiducial parameters, we find  $\mathcal{A}_0 \approx 1.8 \times 10^{-4}$ , one can see in Fig 18. Given that, we can then write

$$w \approx \left[ \frac{\mathcal{A}_0 (x_B q_k^F \ell_p k_0)^2}{A_s} \right]^{2/5}, \quad (97)$$

In practice, the observational comparison is performed by fitting a standard  $\Lambda$ CDM cosmological model, with the sole modification that the primordial curvature power spectrum is replaced by the two-fluid spectrum described in this work. All late-time physics—including the background expansion, recombination, and radiative transfer—is treated as in  $\Lambda$ CDM, while the effects of the contracting two-fluid phase enter exclusively through the primordial initial conditions encoded in  $\mathcal{P}_\zeta(k)$ . This allows for a direct and consistent comparison with CMB data using standard Boltzmann solvers.

Using the above parametrization, we obtain a representative fit to the Planck 2018 data (baseline temperature and polarization: TT-TE-EE + low- $\ell$ ) [35], yielding

$$H_0 = 69.56 \text{ km s}^{-1} \text{ Mpc}^{-1}, \quad (98a)$$

$$A_s = 2.16 \times 10^{-9}, \quad (98b)$$

$$k_0 = 1.93 \times 10^{-3} \text{ Mpc}^{-1}. \quad (98c)$$

These values correspond to the inferred physical parameters

$$\Omega_r = 1.45 \times 10^{-7}, \quad (99a)$$

$$w = 9.44 \times 10^{-22} \left( \frac{x_B}{10^{30}} \right)^{4/5}. \quad (99b)$$

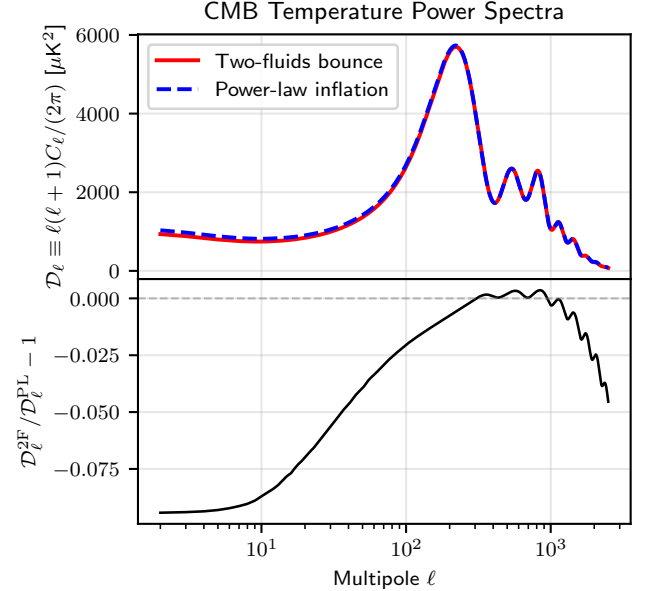


Figure 19. Comparison of the CMB angular power spectrum  $\ell(\ell+1)C_\ell/(2\pi)$  obtained from the two-fluid primordial spectrum (solid line) with that derived from a standard power-law spectrum (dashed line). Over most of the multipole range, the two models show good agreement, with the two-fluid model predicting slightly reduced power at the largest and smallest scales, at the level of at most  $\sim 8\%$ .

This, in turn, yields an asymmetry parameter  $\gamma_{\text{assym}} = 0.13$ , consistent with the estimate obtained earlier.

In Fig. 19, we show the resulting CMB angular power spectrum  $C_\ell$  computed using the CLASS Boltzmann solver [40] with the above best-fit parameters, compared to the standard power-law primordial spectrum fitted to the same data set.

Overall, this comparison demonstrates that the primordial power spectrum generated by the contracting two-fluid model can be consistently embedded within the standard  $\Lambda$ CDM framework and yields CMB angular power spectra compatible with current observations. While a full statistical exploration of the parameter space is beyond the scope of the present work, these results establish the phenomenological viability of the model and provide a solid foundation for a dedicated follow-up analysis focusing on parameter inference and observational constraints.

## CONCLUSIONS

In this work, we proposed and discussed an effective two fluid quantum cosmological model in the framework of Canonical Quantum Gravity using a proper definition of quantum trajectories, from which we extracted wavefunctions and their corresponding non-singular quantum scale factor evolutions and perturbations. The two fluids

we considered are an almost (but not quite) pressureless fluid and radiation. We performed an analysis for both background and perturbations, generalizing the literature on bouncing models. At perturbative level, perturbations were quantized using the coupled adiabatic vacuum prescription: Hamiltonian diagonalization followed by the adiabatic expansion up to second order.

Concerning the predictions, at background level, the obtained scale factor is non-singular and presents a bounce. At perturbative level the obtained adiabatic primordial power spectrum presents a red-tilt, which is non-trivial to implement in single fluid bouncing models. Furthermore, the contracting phase acts as a dynamical mechanism that amplifies adiabatic perturbations without generating large entropy perturbations, which explains the absence of isocurvature perturbations on the CMB without fine-tuning nor need to postulate special initial conditions, as is often performed in multi-field inflationary models.

Additional theoretical advantages arise due to the fact that, since this model does not contain an inflationary phase, there is no need to postulate a reheating phase where physics is unknown, nor are there any trans-Planckian frequencies that impact the CMB. Furthermore, due to the use of the de Broglie-Bohm interpretation of quantum mechanics to extract trajectories associated to wavefunctions, there is no quantum-to-classical transition problem.

Regarding observational constraints for this model, since the adiabatic power spectrum is not an exact power law, one must perform a full MCMC analysis of CMB data to derive the best fit parameters and confidence regions. This was originally intended to be performed for this work, but the MCMC analysis of Planck Temperature + lowE data lead to an interesting, non-trivial result: the Hubble constant value  $H_0$  determined by the CMB was increased using this power spectrum, so that the model offers an alleviation for the well known Hubble Tension problem.

Because of these considerations, the MCMC analysis based on cosmological survey data is presented separately in the companion paper Two Fluid Quantum Bouncing Cosmology Part II: Observational Constraints [41]. A preliminary assessment suggests that the model can match current CMB and LSS observations in specific regions of parameter space, while showing indications of reducing the  $H_0$  and  $\sigma_8$  tensions. If these results are confirmed by the full analysis in Part II, the model may represent a non-singular scenario capable of producing the primordial power spectrum without invoking exotic matter, while remaining compatible with existing cosmological constraints.

It should also be of note that, provided the bounce occurs rapidly enough, the perturbative predictions of bouncing models differ only in the relation of the amplitude to the bounce scale,  $a_B$ . Therefore, two fluid models with different bouncing mechanisms, e.g. , Loop Quantum Cosmology, would lead to similar predictions,

defining a class of models that could be considered competitive alternatives to inflationary models. Finally, if one considers the specific bouncing mechanism of canonical quantization through the Wheeler-De Witt equation, this model then leads to constraints on effective models of canonical quantum gravity using cosmological data.

While the model already displays several interesting features, it is still simple in the sense that it contains only two fluids; dark energy has not been included, for example. Future work can then be based on the implementation of dark energy in the contracting phase, which would demand still more advanced theoretical techniques, in particular with regards to the definition of an appropriate vacuum state [29, 30]. Furthermore, because the model remains consistent with the constraints considered so far, further observational tests are also of interest. In particular, observations that could probe the radiation domination region of the spectrum where it grows due to the blue tilt become relevant. In this regard, spectral distortions, the production of primordial black holes, primordial gravitational waves and further LSS constraints seem promising, which we intend to address in future work.

## ACKNOWLEDGMENTS

This work is supported by Conselho Nacional de Desenvolvimento Científico e Tecnológico (CNPq) – Brasil. NPN acknowledges the support of CNPq of Brazil under grant PQ-IB 310121/2021-3. LFD acknowledges the support of CAPES under the grant DS 88887.902808/2023-00.

## Appendix A: Adiabatic Approximation for the Two-Fluid System

In the contracting phase of our model, the perturbations are described by two coupled degrees of freedom,  $(\zeta, Q)$ , associated with the two fluids. Quantizing this system requires a choice of basis functions for the mode expansion. A natural starting point is to identify an *instantaneous* set of oscillatory solutions, so that each mode can be followed as the background evolves. The adiabatic approximation provides a systematic way to construct such a basis when the background changes slowly compared to the oscillation timescale.

Defining the components of the phase-space vector by setting

$$y^a \doteq (\zeta, Q, \Pi_\zeta, \Pi_Q), \quad (A1)$$

we write the equations of motion in matrix form

$$\dot{y}^a = M^a{}_b(\alpha) y^b, \quad (A2)$$

with the evolution matrix  $M^a_b(\alpha)$  given by

$$M^a_b \doteq \begin{pmatrix} 0 & 0 & \frac{c_\zeta^2}{\gamma} & \frac{s\Delta c^2\gamma_r\gamma_w}{\gamma^2} \\ 0 & 0 & \frac{s\Delta c^2\gamma_r\gamma_w}{\gamma^2} & \frac{\gamma_w\gamma_r c_Q^2}{\gamma^2} \\ -\gamma F_\nu^2 & 0 & 0 & 0 \\ 0 & -\frac{\gamma F_\nu^2}{\gamma_r\gamma_w} & 0 & 0 \end{pmatrix}. \quad (\text{A3})$$

If the background evolves on a timescale much longer than a typical oscillation period, we may try a leading-order Wentzel-Kramers-Brillouin (WKB)-type solution:

$$\bar{y}_i^a(\alpha) \equiv e^{-i \int \nu_i(\tilde{\alpha}) d\tilde{\alpha}} v_i^a(\alpha), \quad (\text{A4})$$

where  $i = 1, 2$  labels two complex linearly independent solutions,  $v_i^a(\alpha)$  representing the corresponding eigenvectors of the evolution matrix (A3) whose eigenvalues  $\nu_i(\alpha) \in \mathbb{R}$ , given by

$$\nu_1 = c_r F_\nu, \quad \nu_2 = c_w F_\nu. \quad (\text{A5})$$

play the role of instantaneous frequencies.

The instantaneous eigenmodes are thus defined by

$$M^a_b(\alpha) v_i^b(\alpha) = -i \nu_i(\alpha) v_i^a(\alpha), \quad (\text{A6})$$

(no sum) with

$$v_i^a(\alpha) \doteq (\bar{\zeta}_i, \bar{Q}_i, \bar{\Pi}_{\zeta i}, \bar{\Pi}_{Q i}). \quad (\text{A7})$$

Substituting the ansatz into (A2) yields

$$\dot{\bar{y}}_i^a = (-i \nu_i v_i^a + \dot{v}_i^a) e^{-i \int \nu_i d\alpha} = M^a_b v_i^b e^{-i \int \nu_i d\alpha}. \quad (\text{A8})$$

At leading order in the adiabatic approximation, the variation of  $v_i^a$  is neglected, i.e.  $\dot{v}_i^a \approx 0$ . This corresponds to treating each eigenvector as fixed while its phase oscillates with frequency  $\nu_i$ .

In reality,  $M^a_b$  depends on background quantities and is therefore time-dependent, so  $v_i^a(\alpha)$  changes slowly. In the WKB expansion, this time variation generates mode mixing through the correction term  $\dot{v}_i^a$ . The adiabatic approximation is valid when these corrections are small: assuming a characteristic time  $T$  for the evolution of  $v_i^a$ , i.e.  $[\dot{v}_i^a] \simeq v_i^a/T$ , our adiabatic approximation is valid provided  $T \gg \nu_i^{-1}$ , which requires that the background evolve on timescales much longer than the oscillation period of each mode.

As shown in Ref. [17], the matrix  $M^a_b$  has two pairs of complex-conjugate eigenvalues. Each pair corresponds to one of the two physical oscillation frequencies (A5) of the coupled system: one propagating with the speed-of-sound of the radiation component,  $c_r$ , and the other with the speed-of-sound of the cold-matter-like component,  $c_w = \sqrt{w}$ . A convenient choice of normalized eigenvectors (up to an overall phase) is

$$v_1^a \doteq \left( s \sqrt{\frac{c_r \gamma_r}{2F_\nu \gamma^2}}, \sqrt{\frac{c_r \gamma_r}{2F_\nu \gamma^2}} \gamma_w, -is \sqrt{\frac{\gamma_r F_\nu}{2c_r}}, -i \sqrt{\frac{F_\nu}{2c_r \gamma_r}} \right), \quad (\text{A9})$$

and

$$v_2^a \doteq \left( -s \sqrt{\frac{c_w \gamma_w}{2F_\nu \gamma^2}}, \sqrt{\frac{c_w \gamma_w}{2F_\nu \gamma^2}} \gamma_r, is \sqrt{\frac{\gamma_w F_\nu}{2c_w}}, -i \sqrt{\frac{F_\nu}{2c_w \gamma_w}} \right). \quad (\text{A10})$$

The other two eigenvectors are the complex conjugates of the above, with respective eigenvalues  $-\nu_1$  and  $-\nu_2$ .

To compute products between eigenvectors (or between any solutions of the system), we introduce the symplectic matrix

$$\Omega_{ab} \doteq \begin{pmatrix} 0 & 0 & 1 & 0 \\ 0 & 0 & 0 & 1 \\ -1 & 0 & 0 & 0 \\ 0 & -1 & 0 & 0 \end{pmatrix}, \quad (\text{A11})$$

which we use to define the Wronskian between  $v_i$  and  $v_j$  through

$$W(v_i, v_j) \equiv v_i^{a*} \Omega_{ab} v_j^b, \quad (\text{A12})$$

and the eigenvectors are normalized by the statement

$$W(v_i, v_j) = -i \delta_{ij}, \quad (\text{A13})$$

a condition that fixes the normalization for the quantum creation and annihilation operators and, in the classical theory, provides a complete orthonormal basis. Moreover, since the eigenvectors are mutually orthogonal, we have

$$W(v_i^*, v_j) = 0, \quad (\text{A14})$$

The mode functions obtained by evolving these normalized eigenvectors and including the adiabatic corrections described below reproduce exactly the vacuum choice of Ref. [17]. Thus, the set  $\{v_k^a, v_k^{a*}\}$  forms a complete instantaneous basis for the four-dimensional phase space in terms of which one can decompose any vector.

To account for the slow time dependence of the eigenvectors  $v_i^a(\alpha)$ , we extend the leading-order WKB ansatz by including a first-order correction

$$y_i^a(\alpha) = e^{-i \int \nu_i(\tilde{\alpha}) d\tilde{\alpha}} [v_i^a(\alpha) + u_i^a(\alpha)], \quad (\text{A15})$$

where  $u_i^a(\alpha)$  describes the deviation from the instantaneous-eigenvector solution induced by the slow evolution of the background.

Substituting this ansatz into the system (A2) and keeping only first-order terms in the adiabatic expansion gives

$$(M^a_b + i\nu_i \delta^a_b) u_i^b(\alpha) = \dot{v}_i^a(\alpha) + \dot{u}_i^a(\alpha) \approx \dot{v}_i^a(\alpha), \quad (\text{A16})$$

where, in the last step, we neglected  $\dot{u}_i^a$  since it is of second order in the adiabatic parameter. The time derivative of the instantaneous eigenvector,  $\dot{v}_i^a(\alpha)$ , therefore acts as a known source term for the correction  $u_i^a(\alpha)$ .

Obtaining the first order correction  $u_i^a(\alpha)$  through Eq. (A16) requires to invert the operator  $M^a_b + i\nu_i \delta^a_b$ .

Seen as acting in the full 4-dimensional space of configurations, this operator is however not invertible since the instantaneous eigenvector  $v_i^a$  lies in its kernel. The three remaining eigenvectors  $v_{k \neq i}^a$  and  $v_k^{a*}$ , i.e. the other positive-frequency mode and the two negative-frequency modes, are also eigenvectors of this operator, with respective eigenvalues  $-(\nu_k - \nu_i)$  and  $i(\nu_k + \nu_i)$ , and are linearly independent. They span the three-dimensional subspace orthogonal to  $v_i^a$  with respect to the symplectic product, subspace in which the source term  $\dot{v}_i$  should lie, so we also demand  $W(\dot{v}_i, v_i) = 0$ , a condition that can be enforced by an appropriate choice of phase for  $v_i^a$ .

To express this orthogonality condition explicitly, we exploit the fact that the set  $\{v_k^a, v_k^{a*}\}$  forms a complete instantaneous basis for the four-dimensional phase space. We can thus decompose<sup>5</sup> the time derivative of  $v_i^a$  as

$$\dot{v}_i^a = \alpha_i^k v_k^a + \beta_i^k v_k^{a*}, \quad (\text{A17})$$

where the sum over  $k$  runs over the two frequency modes.

Taking the derivative of the orthonormality conditions Eqs. (A13) and (A14) with respect to  $\alpha$  and substituting the above decomposition yields the constraints

$$\alpha_{ij}^* + \alpha_{ji} = 0, \quad \beta_{ij} - \beta_{ji} = 0. \quad (\text{A18})$$

Since  $\alpha_{ii}$  is purely imaginary, it represents a phase rotation that can be absorbed by redefining the phase of  $v_i^a$ . Moreover, we impose the gauge choice  $\alpha_{ii} = 0$ , ensuring  $W(\dot{v}_i, v_i) = 0$ . The remaining coefficients  $\alpha_{ij}$  ( $i \neq j$ ) and  $\beta_{ij}$  describe physical mode mixing and particle production.

When the first-order correction  $u_i^a$  is included, the orthonormality conditions (A13) and (A14) applied to  $y_i^a = v_i^a + u_i^a$  imply, to first order,

$$W(u_i, v_j) + W(v_i, u_j) \approx 0 \quad (\text{A19})$$

and

$$W(u_i^*, v_j) + W(v_i^*, u_j) \approx 0. \quad (\text{A20})$$

Decomposing  $u_i^a = \mathfrak{a}_i^k v_k^a + \mathfrak{b}_i^k v_k^{a*}$ , one recovers Eq. (A18) with the substitution  $\alpha_{ij} \rightarrow \mathfrak{a}_{ij}$  and  $\beta_{ij} \rightarrow \mathfrak{b}_{ij}$ . In particular,  $\mathfrak{a}_{ii}$  is purely imaginary and can be absorbed by a (first order) phase redefinition, leaving  $W(u_i, v_i) = 0$ . Thus both  $\dot{v}_i^a$  and  $u_i^a$  lie in the three-dimensional subspace orthogonal to  $v_i^a$ , i.e.  $W(\dot{v}_i, v_i) = 0$  and  $W(u_i, v_i) = 0$ .

Since both  $\dot{v}_i^a$  and  $u_i^a$  lie in the orthogonal subspace, we can explicitly invert the operator on this subspace.<sup>6</sup> For  $i = 1$ , the inverse takes the form

$$(M^a{}_b + i\nu_1 \delta^a{}_b)^{-1} = - \left( \frac{v_1^{a*} v_1^c}{2\nu_1} + \frac{v_2^a v_2^{c*}}{\nu_2 - \nu_1} + \frac{v_2^{a*} v_2^c}{\nu_2 + \nu_1} \right) \Omega_{cb}, \quad (\text{A21})$$

<sup>5</sup> Note we write the coefficients as  $\alpha_{ij}$  and  $\beta_{ij}$  to match with the usual notation for such a Bogoliubov expansion, but the first coefficient should not be confused with our time parameter  $\alpha$ .

<sup>6</sup> Naturally, if we apply the inverse to the original operator, we obtain the projector onto the orthogonal subspace. That is, the

which is used to obtain  $u_1^a(\alpha)$ . This generalizes the standard WKB prefactor for a single mode  $1/(2\nu_i)$  and allows to include the full spectral structure, with denominators given by differences between  $\nu_1$  and the remaining eigenvalues.

### 1. Explicit form of the first-order corrections

To make the size of the first-order correction explicit, we factor it relative to each component of the leading-order mode. For the  $i$ -th mode we write

$$\begin{aligned} v_i^1 + u_i^1 &= \bar{\zeta}_i (1 + \delta_{\zeta_i}), & v_i^2 + u_i^2 &= \bar{Q}_i (1 + \delta_{Q_i}), \\ v_i^3 + u_i^3 &= \bar{\Pi}_{\zeta i} (1 + \delta_{\Pi_{\zeta i}}), & v_i^4 + u_i^4 &= \bar{\Pi}_{Q i} (1 + \delta_{\Pi_{Q i}}), \end{aligned}$$

where  $\delta_{\zeta_i}$ ,  $\delta_{Q_i}$ ,  $\delta_{\Pi_{\zeta i}}$  and  $\delta_{\Pi_{Q i}}$  are complex functions of  $\alpha$  describing the relative correction to each component. By construction, one has  $\delta_{\zeta_i} \equiv u_i^1/v_i^1$ ,  $\delta_{Q_i} \equiv u_i^2/v_i^2$ ,  $\delta_{\Pi_{\zeta i}} \equiv u_i^3/v_i^3$  and  $\delta_{\Pi_{Q i}} \equiv u_i^4/v_i^4$ . This notation allows us to track amplitude and phase shifts for each physical quantity ( $\zeta, Q, \Pi_\zeta, \Pi_Q$ ) separately, and to identify which components are most affected by adiabaticity violations. These corrections depend on time derivatives of the background functions:

$$\frac{\dot{\gamma}_i}{\gamma_i} = -3s c_i^2 + \frac{\dot{N}}{N}, \quad \frac{\dot{F}_\nu}{F_\nu} = \frac{\dot{N}}{N} - s. \quad (\text{A22})$$

Using these relations, the corrections for the first eigenmode are:

$$\delta_{\zeta_1} = \frac{1}{2i c_r F_\nu} \left[ \frac{s}{2} \left( 3c_r^2 - 1 - \frac{6c_r^2 \gamma_r}{\gamma} \right) + \frac{\dot{N}}{N} \left( 2 - \frac{\gamma_r}{\gamma} \right) \right], \quad (\text{A23a})$$

$$\delta_{Q_1} = \frac{1}{2i c_r F_\nu} \left[ \frac{s}{2} \left( 3c_r^2 - 1 - \frac{6c_r^2 \gamma_r}{\gamma} \right) - \frac{\dot{N} \gamma_r}{N \gamma} \right], \quad (\text{A23b})$$

$$\delta_{\Pi_{\zeta 1}} = \frac{1}{2i c_r F_\nu} \left[ \frac{s}{2} \left( 9c_r^2 + 1 - \frac{6c_r^2 \gamma_r}{\gamma} \right) - \frac{\dot{N} \gamma_r}{N \gamma} \right], \quad (\text{A23c})$$

$$\delta_{\Pi_{Q 1}} = \frac{1}{2i c_r F_\nu} \left[ \frac{s}{2} \left( -3c_r^2 + 1 - \frac{6c_r^2 \gamma_r}{\gamma} \right) - \frac{\dot{N} \gamma_r}{N \gamma} \right]. \quad (\text{A23d})$$

partition of the identity given by

$$\delta^a{}_b = -i \sum_{k=1}^2 (v_k^{a*} v_k^c - v_k^a v_k^{c*}) \Omega_{cb}.$$

and the inverse operator satisfy

$$(M^a{}_c + i\nu_i \delta^a{}_c) (M^c{}_b + i\nu_i \delta^c{}_b)^{-1} = \delta^a{}_b - i v_i^a v_i^{c*} \Omega_{cb}.$$

and for the second eigenmode:

$$\delta_{\zeta_2} = \frac{1}{2ic_w F_\nu} \left[ \frac{s}{2} \left( -3c_w^2 - 1 + \frac{6c_w^2 \gamma_r}{\gamma} \right) + \frac{\dot{N}}{N} \left( 1 + \frac{\gamma_r}{\gamma} \right) \right], \quad (\text{A24a})$$

$$\delta_{Q_2} = \frac{1}{2ic_w F_\nu} \left[ \frac{s}{2} \left( -3c_w^2 - 1 + \frac{6c_w^2 \gamma_r}{\gamma} \right) - \frac{\dot{N}}{N} \frac{\gamma_r}{\gamma} \right], \quad (\text{A24b})$$

$$\delta_{\Pi_{\zeta_2}} = \frac{1}{2ic_w F_\nu} \left[ \frac{s}{2} \left( 3c_w^2 + 1 + \frac{6c_w^2 \gamma_r}{\gamma} \right) - \frac{\dot{N}}{N} \frac{\gamma_r}{\gamma} \right], \quad (\text{A24c})$$

$$\delta_{\Pi_{Q_2}} = \frac{1}{2ic_w F_\nu} \left[ \frac{s}{2} \left( -9c_w^2 + 1 + \frac{6c_w^2 \gamma_r}{\gamma} \right) - \frac{\dot{N}}{N} \frac{\gamma_r}{\gamma} \right]. \quad (\text{A24d})$$

The dominant parameter controlling the magnitude of the corrections above is  $(c_i F_\nu)^{-1}$ , which can be rewritten as

$$\frac{1}{c_i F_\nu} = \frac{a|H|}{c_i k_c} = \frac{a \lambda_c}{c_i R_H}.$$

Here,  $\lambda \equiv 1/k$  is the comoving wavelength and  $R_H \equiv 1/|H|$  is the Hubble radius. The factor  $c_i$  accounts for the propagation speed of the mode, so this ratio measures the physical wavelength (including the sound speed) relative to the Hubble radius.

This quantity determines the regime of validity of the WKB approximation: when  $c_i F_\nu \gg 1$ , the mode oscillates on a timescale much shorter than the Hubble time, and the first-order corrections remain small.

Additionally, the remaining factors in the corrections are either of order unity or involve the ratio  $\gamma_r/\gamma$ . During the radiation-dominated phase this ratio is of order unity, while during matter domination it is subdominant by definition: although it grows in the contracting phase as  $a^{-1+3w} \sim 1/a$ , its amplitude remains small, ensuring that the first-order corrections remain controlled and adiabaticity is preserved at late times. After the transition

to the radiation era, these factors either stabilize at order unity or decay.

To estimate the truncation error of the adiabatic approximation, we extend the perturbative expansion to include the second-order correction  $q_i^a$ ,

$$y_i^a = v_i^a + u_i^a + q_i^a,$$

where  $u_i^a$  is the first-order term and  $q_i^a$  is the second-order term in the adiabatic expansion. For example, for the first component,

$$v_i^1 + u_i^1 + q_i^1 = \bar{\zeta}_i \left[ 1 + \delta_{\zeta_i} + \delta_{\zeta_i}^{(2)} \right],$$

where  $\delta_{\zeta_i} \equiv u_i^1/v_i^1$  is the first-order relative correction and  $\delta_{\zeta_i}^{(2)} \equiv q_i^1/v_i^1$  is the second-order term. The same definition applies to all other components.

The explicit forms of  $\delta^{(2)}$  are lengthy and omitted here, but are implemented in the numerical code used to generate the plots. In practice, we compute  $\delta_{\zeta_i}$  and  $\delta_{\zeta_i}^{(2)}$  analytically, and estimate the third-order term as the product  $\delta_{\zeta_i} \delta_{\zeta_i}^{(2)}$ . Since the adiabatic approximation must hold for all components simultaneously, we define the adiabatic scale

$$\Delta_{\zeta_i} = \left| \delta_{\zeta_i} \delta_{\zeta_i}^{(2)} \right|^{1/3}, \quad (\text{A25})$$

with no summation over repeated  $i$ . This scale varies as  $c_i F_\nu$ , as discussed earlier. The time at which the adiabatic approximation introduces a truncation error of order  $\epsilon$  is determined numerically by solving

$$\Delta_{\zeta_i}^3 + \Delta_{Q_i}^3 + \Delta_{\Pi_{\zeta_i}}^3 + \Delta_{\Pi_{Q_i}}^3 = \epsilon.$$

This criterion provides a conservative estimate of the truncation error, and we have verified through numerical integrations that it consistently overestimates the actual error. From that point onward, the evolution is computed by directly integrating the full coupled system.

---

[1] F. Finelli and R. Brandenberger, [Generation of a scale-invariant spectrum of adiabatic fluctuations in cosmological models with a contracting phase](#), Phys. Rev. D **65**, 103522 (2002).

[2] L. E. Allen and D. Wands, [Cosmological perturbations through a simple bounce](#), Phys. Rev. D **70**, 063515 (2004).

[3] P. Peter, E. J. Pinho, and N. Pinto-Neto, A Non inflationary model with scale invariant cosmological perturbations, Phys. Rev. D **75**, 023516 (2007), [arXiv:hep-th/0610205 \[hep-th\]](#).

[4] D. Wands, Duality invariance of cosmological perturbation spectra, Phys. Rev. D **60**, 023507 (1999), [arXiv:9809062 \[gr-qc\]](#).

[5] L. F. Guimaraes, F. T. Falciano, and G. Brando, A quasi-matter bounce equivalent to starobinsky inflation, Phys. Rev. D **99**, 103515 (2019), [arXiv:1902.05031](#).

[6] A. P. Bacalhau, N. Pinto-Neto, and S. Dias Pinto Vintenti, Consistent Scalar and Tensor Perturbation Power Spectra in Single Fluid Matter Bounce with Dark Energy Era, Phys. Rev. D **97**, 083517 (2018), [arXiv:1706.08830 \[gr-qc\]](#).

[7] C. Kiefer, [Quantum Gravity](#), International Series of Monographs on Physics (Oxford University Press, 2025).

[8] M. Bojowald, Loop quantum cosmology, Living Rev. Rel. **8**, 11 (2005), [arXiv:gr-qc/0601085](#).

[9] R. B. Neves, *Observational imprints from Loop Quantum Cosmology* Other thesis, Universidad Complutense de Madrid (2024), [arXiv:2410.14435 \[gr-qc\]](https://arxiv.org/abs/2410.14435).

[10] R. Brandenberger, Superstring cosmology — a complementary review, *JCAP* **11** (11), 019, [arXiv:2306.12458 \[hep-th\]](https://arxiv.org/abs/2306.12458).

[11] L. Chataignier, C. Kiefer, and P. Moniz, Observations in quantum cosmology, *Class. Quant. Grav.* **40**, 223001 (2023), [arXiv:2306.14948 \[gr-qc\]](https://arxiv.org/abs/2306.14948).

[12] P. Peter, E. Pinho, and N. Pinto-Neto, Tensor perturbations in quantum cosmological backgrounds, *JCAP* **07** (07), 014, [arXiv:hep-th/0509232](https://arxiv.org/abs/hep-th/0509232).

[13] P. Peter, E. J. C. Pinho, and N. Pinto-Neto, Gravitational wave background in perfect fluid quantum cosmologies, *Phys. Rev. D* **73**, 104017 (2006), [arXiv:gr-qc/0605060](https://arxiv.org/abs/gr-qc/0605060).

[14] F. T. Falciano and N. Pinto-Neto, Scalar Perturbations in Scalar Field Quantum Cosmology, *Phys. Rev. D* **79**, 023507 (2009), [arXiv:0810.3542 \[gr-qc\]](https://arxiv.org/abs/0810.3542).

[15] S. D. P. Vitenti, F. T. Falciano, and N. Pinto-Neto, Quantum Cosmological Perturbations of Generic Fluids in Quantum Universes, *Phys. Rev. D* **87**, 103503 (2013), [arXiv:1206.4374 \[gr-qc\]](https://arxiv.org/abs/1206.4374).

[16] F. T. Falciano, N. Pinto-Neto, and S. Dias Pinto Vitenti, Scalar Field Perturbations with Arbitrary Potentials in Quantum Backgrounds, *Phys. Rev. D* **87**, 103514 (2013), [arXiv:1305.4664 \[gr-qc\]](https://arxiv.org/abs/1305.4664).

[17] P. Peter, N. Pinto-Neto, and S. D. P. Vitenti, Quantum Cosmological Perturbations of Multiple Fluids, *Phys. Rev. D* **93**, 023520 (2016), [arXiv:1510.06628 \[gr-qc\]](https://arxiv.org/abs/1510.06628).

[18] J. Acacio de Barros, N. Pinto-Neto, and M. A. Sagioro-Leal, The Causal interpretation of dust and radiation fluids nonsingular quantum cosmologies, *Phys. Lett. A* **241**, 229 (1998), [arXiv:gr-qc/9710084 \[gr-qc\]](https://arxiv.org/abs/gr-qc/9710084).

[19] N. Pinto-Neto and J. C. Fabris, Quantum cosmology from the de Broglie-Bohm perspective, *Class. Quant. Grav.* **30**, 143001 (2013), [arXiv:1306.0820 \[gr-qc\]](https://arxiv.org/abs/1306.0820).

[20] P. Małkiewicz, P. Peter, and S. D. P. Vitenti, Quantum empty Bianchi I spacetime with internal time, *Phys. Rev. D* **101**, 046012 (2020), [arXiv:1911.09892 \[gr-qc\]](https://arxiv.org/abs/1911.09892).

[21] J. d. C. Martin, P. Małkiewicz, and P. Peter, Unitarily inequivalent quantum cosmological bouncing models, *Phys. Rev. D* (2021), [arXiv:2111.02963 \[gr-qc\]](https://arxiv.org/abs/2111.02963).

[22] K. Mazzle, L. Mickel, and P. Peter, Quantum cosmological background superposition and perturbation predictions (2025), [arXiv:2508.06231 \[gr-qc\]](https://arxiv.org/abs/2508.06231).

[23] L. de Broglie, La mécanique ondulatoire et la structure atomique de la matière, *J. Phys. Radium* **8**, 225 (1927).

[24] D. Bohm, A Suggested interpretation of the quantum theory in terms of hidden variables. 1., *Phys. Rev.* **85**, 166 (1952).

[25] D. Bohm, A Suggested interpretation of the quantum theory in terms of hidden variables. 2., *Phys. Rev.* **85**, 180 (1952).

[26] J. Acacio de Barros and N. Pinto-Neto, The causal interpretation of quantum mechanics and the singularity problem and time issue in quantum cosmology, *Int. J. Mod. Phys. D* **7**, 201 (1998).

[27] R. Holland, The de Broglie-Bohm theory of motion and quantum field theory, *Phys. Rept.* **224**, 95 (1993).

[28] N. Pinto-Neto, E. S. Santini, and F. T. Falciano, Quantization of Friedmann cosmological models with two fluids: Dust plus radiation, *Phys. Lett. A* **344**, 131 (2005), [arXiv:gr-qc/0505109](https://arxiv.org/abs/gr-qc/0505109).

[29] R. Maier, S. Pereira, N. Pinto-Neto, and B. B. Siffert, Bouncing models with a cosmological constant, *Physical Review D—Particles, Fields, Gravitation, and Cosmology* **85**, 023508 (2012).

[30] M. Penna-Lima, N. Pinto-Neto, and S. D. P. Vitenti, New formalism to define vacuum states for scalar fields in curved space-times, *Phys. Rev. D* (2022), [arXiv:2207.08270 \[gr-qc\]](https://arxiv.org/abs/2207.08270).

[31] S. Vitenti, F. Falciano, and N. Pinto-Neto, Quantum cosmological perturbations of generic fluids in quantum universes, *Physical Review D—Particles, Fields, Gravitation, and Cosmology* **87**, 103503 (2013).

[32] B. F. Schutz, Perfect Fluids in General Relativity: Velocity Potentials and a Variational Principle, *Phys. Rev. D* **2**, 2762 (1970).

[33] P. Peter and J.-P. Uzan, *Primordial Cosmology*, Oxford Graduate Texts (Oxford University Press, 2013).

[34] S. D. P. Vitenti and N. Pinto-Neto, Large adiabatic scalar perturbations in a regular bouncing universe, *Physical Review D—Particles, Fields, Gravitation, and Cosmology* **85**, 023524 (2012).

[35] Planck Collaboration, N. Aghanim, Y. Akrami, M. Ashdown, J. Aumont, C. Baccigalupi, M. Ballardini, A. J. Banday, R. B. Barreiro, N. Bartolo, S. Basak, et al., Planck 2018 results. VI. Cosmological parameters, *Astronomy & Astrophysics* **641**, A6 (2020), [arXiv:1807.06209 \[astro-ph.CO\]](https://arxiv.org/abs/1807.06209).

[36] Planck Collaboration, Y. Akrami, F. Arroja, M. Ashdown, J. Aumont, C. Baccigalupi, M. Ballardini, A. J. Banday, R. Barreiro, N. Bartolo, S. Basak, et al., Planck 2018 results-x. constraints on inflation, *Astronomy & Astrophysics* **641**, A10 (2020).

[37] D. Bessada, N. Pinto-Neto, B. B. Siffert, and O. D. Miranda, Stochastic background of relic gravitons in a bouncing quantum cosmological model, *Journal of Cosmology and Astroparticle Physics* **2012** (11), 054.

[38] A. P. Bacalhau, N. Pinto-Neto, and S. D. P. Vitenti, Consistent scalar and tensor perturbation power spectra in single fluid matter bounce with dark energy era, *Physical Review D* **97**, 083517 (2018).

[39] A. Michel and P. Peter, Quantum cosmological gravitational waves?, in *Handbook of Quantum Gravity*, edited by C. Bambi, L. Modesto, and I. Shapiro (Springer Nature Singapore, Singapore, 2023) pp. 1–66.

[40] D. Blas, J. Lesgourgues, and T. Tram, The Cosmic Linear Anisotropy Solving System (CLASS). Part II: Approximation schemes, *J. Cosmol. Astropart. Phys.* **2011** (7), 034, [arXiv:1104.2933 \[astro-ph.CO\]](https://arxiv.org/abs/1104.2933).

[41] S. Vitenti, N. Pinto-Neto, P. Peter, and L. F. Demétrio, Two fluid quantum bouncing cosmology part ii: Observational constraints, In Preparation. (2024).